Article

Cell-Resolved PV Soiling Measurement Using Drone Images

Peter Winkel [1,2,*], Stefan Wilbert [1], Marc Röger [1], Julian J. Krauth [1], Niels Algner [1], Bijan Nouri [1], Fabian Wolfertstetter [3], Jose Antonio Carballo [4], M. Carmen Alonso-Garcia [5], Jesus Polo [5], Aránzazu Fernández-García [2] and Robert Pitz-Paal [2,6]

1   German Aerospace Center (DLR), Institute of Solar Research, Calle Doctor Carracido 44, 04005 Almería, Spain
2   Chair of Solar Technology, Faculty of Mechanical Engineering, RWTH Aachen University, Linder Höhe, 51147 Cologne, Germany; robert.pitz-paal@dlr.de (R.P.-P.)
3   Volateq GmbH, Mühlenhof 7-9, 40721 Hilden, Germany
4   CIEMAT, Plataforma Solar de Almería, Carretera de Senés km 4, 04200 Tabernas, Spain; joseantonio.carballo@psa.es
5   CIEMAT, Photovoltaic Solar Energy Unit, Av. Complutense 40, 28040 Madrid, Spain; jesus.polo@ciemat.es (J.P.)
6   DLR, Institute of Solar Research, Linder Höhe, 51147 Cologne, Germany
*   Correspondence: peter.winkel@dlr.de

Abstract: The maintenance of photovoltaic (PV) power plants is of central importance for their yield. To reach higher efficiencies in PV parks, it is helpful to detect soiling such as dust deposition and to apply this information to optimize cleaning strategies. Furthermore, a periodic inspection of the PV modules with infrared (IR) imagery is of advantage to detect and potentially remove faulty PV modules. Soiling can be erroneously interpreted as PV module defects and hence spatially resolved soiling measurements can improve the results of IR-based PV inspection. So far, soiling measurements are mostly performed only locally in PV fields, thus not supporting the above-mentioned IR inspections. This study presents a method for measuring the soiling of PV modules at cell resolution using RGB images taken by aerial drones under sunny conditions. The increase in brightness observed for soiled cells under evaluation, compared to clean cells, is used to calculate the transmission loss of the soiling layer. Photos of a clean PV module and a soiled module for which the soiling loss is measured electrically are used to determine the relation between the brightness increase and the soiling loss. To achieve this, the irradiance at the time of the image acquisitions and the viewing geometry are considered. The measurement method has been validated with electrical measurements of the soiling loss yielding root mean square deviations in the 1% absolute range. The method has the potential to be applied to entire PV parks in the future.

Keywords: soiling; PV soiling measurement; solar energy; drone-based PV monitoring; image-based PV-monitoring

1. Introduction

Transforming the global energy system from one based on fossil fuels to one based on a mix of renewable sources is vital to achieving net zero greenhouse gas emissions by 2050. It is expected that in the new global energy system, solar energy will be one of the largest contributors of renewable energy sources [1,2]. Among the most advanced solar technologies is photovoltaic (PV), which in recent years has undergone great deployment, in many cases large commercial plants. The demand for monitoring PV plants increases as the globally installed PV capacity grows. One of the reasons for monitoring is soiling. The potential energy yield of PV power plants is estimated to be reduced by 3% to 4% due to soiling [3]. This value might increase in the future as more plants are built in dusty areas such as North Africa and the Near East [3]. Note that the impact of soiling is strongly dependent on the location and the arid regions typically show higher soiling losses [4]. Additionally, inhomogeneous soiling leads to electrical mismatch effects on the module

or string level and can even cause hotspots [5]. Inhomogeneous soiling patterns might be caused by dust accumulations in the lower row of cells of a module or by other soiling types like bird droppings. In severe cases, these might result in fire in large-scale PV systems [6,7]. Hotspots might be detected in IR monitoring drone flights and be misinterpreted as defects while their origin is soiling. Furthermore, soiling can accelerate the degradation of the PV modules, either indirectly by an increased temperature or by direct contact of the soiling with the encapsulant [8–12]. If the soiling losses of a PV system are known, these adverse effects can be quantified, and adequate cleaning strategies can be determined. Therefore, a correct characterization of soiling levels could improve plant performance (direct losses due to soiling), reduce degradation (e.g., by hotspots), and help to optimize maintenance actions (cleaning), which contributes to an improvement in the economic indicators of the plant. Consequently, there is an urgent demand to monitor soiling in PV power plants [13,14]. Micheli et al. have published a study that combines some of the above-mentioned aspects [15]. Investigated was a site in Chile. Soiling was observed over a three-year time period. It was found that within the site itself, the soiling rate can vary by a factor of 3. Additionally, for the site of interest, the optimized cleaning strategy was determined to be three times per year, which according to the authors could decrease the generation costs by 4% compared to a suboptimal cleaning strategy, namely two or four times per year.

There are various methods to measure soiling. Firstly, soiling can be determined by electrically measuring PV modules individually as described by Gostein et al. in [16–18]. Thereby, the power or the short circuit current of the soiled module is compared to the one of a clean reference module. This approach presents an accurate real-time soiling measurement. However, it is not feasible to electrically measure every module in a PV plant individually, and keeping the reference module clean is challenging. Consequently, these methods do not supply information about the soiling status of the entire PV surface.

With the second method used in most PV plants, soiling is measured with commercially available optical soiling sensors that only cover small areas [19,20]. Therefore, many sensors would be needed to analyze spatially resolved soiling. Soiling levels in PV parks vary spatially, e.g., depending on the distance from local soiling sources such as roads [21]. Even within a single PV module, the soiling losses vary.

Spatially resolved information can be derived using imaging techniques. Infrared imaging (IR) has already commonly been used during the monitoring of the operation of PV plants for fault detection [22–25]. There are also visible imaging (RGB) and electroluminescence (EL) imaging techniques for monitoring the operation of PV facilities [26,27]. Also, there has been research on image-based soiling measurements in the visible spectral range to consider spatially resolved soiling [28,29]. The images were either captured by static cameras, for example, surveillance cameras, or by unmanned aerial vehicles (drones). There are a few publications that describe how dust can be recognized by classical computer vision methods applied to images captured by static cameras [28,29]. These papers use histogram methods to distinguish clean from soiled PV modules. Typically, for RGB images of clean modules, the blue channel shows far greater values than the red and the green channels. For the case of soiled modules, the average value of these channels comes closer together. Qasem et al. have analyzed drone images to detect dust [26]. The method is based on comparing the homogeneity of different images. Li et al. also used drones and were additionally able to detect snail trails [30]. The method relies on edge detection. Objects lying on the modules are detected. By analyzing the rectangularity of the detected areas, different soiling types can be distinguished. In addition to classical computer vision, Hwang et al. also applied artificial intelligence (AI) methods to detect dust [31]. The above-mentioned studies have detected dust without estimating the power loss caused.

Cavieres et al. have applied AI-based algorithms to surveillance camera images to estimate the range of the power loss of artificially soiled PV modules [32]. Additionally, the soiling types have been categorized. A similar study has been performed by Mehta et al. to predict the power loss more accurately [33], giving a discrete value for the soiling loss

instead of a range. A dataset that contains more than 45,000 images of a soiled PV panel was created. For each image, the electrical power loss has been measured. With this dataset, the authors have developed an AI model that is capable of predicting the power loss of a module just from seeing an image of this module. The approach is very promising and is mainly limited by the training dataset. All images were captured from the same perspective from the same camera of the same module. The module was artificially soiled. The developed model could therefore not simply be applied to any image of a soiled PV module of a given PV park. The dataset was also published which created a great interest among scholars. Yang et al. have developed a similar AI model that is also capable of predicting the soiling loss just from an image of the soiled module [34]. Compared to Mehta et al., the main advantage is that the training data contained images of a PV module that experienced real outdoor conditions in Doha. This increases the applicability. However, otherwise, the study suffers from the same limitations as the work by Mehta et al. The three studies mentioned above analyze images that were captured by static cameras. Consequently, the scalability of their methods to commercial-scale power plants is questionable. It is expected to be too expensive to cover great parts of a PV park with cameras. The dataset used by Mehta et al. contains only images that were captured from one single perspective. The developed AI models likely learned features that correspond only to that specific perspective. To be more generally applicable, the training dataset should already contain labeled images from various perspectives. It is desirable to be able to analyze drone images captured in a whole plant. This would result in many different camera perspectives relative to the modules. Generally speaking, it is also possible to adapt the above-mentioned methods to drone images. To the best of the authors' knowledge, there is no dataset publicly available of soiled PV modules of various perspectives.

This paper presents a new method that is able to detect soiling by dust and other small particles and quantify its losses. It applies a physical approach that relies on analyzing the light that is scattered at the dust particles. Based on the literature review presented in this section, it is possible to highlight the original contributions of this work. To the best of our knowledge, there is no other method that predicts the soiling losses of PV modules with cell resolution in a scalable way using drone images. Also, compared to AI approaches, our new physical approach offers the advantage that there is no need for a large labeled training dataset. Furthermore, the results are probably easier to interpret as a physical method does not rely on a black box. On the other hand, if in the future there was an AI model to be developed, the method presented here could provide training data. The use of drone images offers the potential to apply the method at the commercial power plant level. The output is resolved on a cell level which means that electrical mismatch effects within a module or a string of modules can be considered.

This paper is structured as follows. Section 2 describes the developed method. Section 3 describes the setup and the data acquisition. The results are presented and discussed in Section 4. Section 5 summarizes the results achieved and suggests future works.

2. Methods

2.1. Optical Measurement Principle

PV modules are typically quite dark because they should absorb as much light as possible in order to convert it into electricity. The deposition of particles on their surface leads to light scattering which makes the modules appear brighter. The method is based on measuring this brightness increase and converting it to the soiling loss. The reflectance of a PV module as well as the scattering by the particles both show a strong angular dependence and have to be considered.

The first step of the method requires isolation of the scattering signal from the signal that would be found for a clean module (clean background calibration). Images of a clean module are taken from various perspectives for this purpose. The second step of the method is the conversion of the brightness increase to the soiling loss (scattering calibration). This is carried out using images of a soiled module with known soiling loss from various

perspectives. The soiling loss of this module is obtained by comparing its power output to that of the cleaned module as described, e.g., in [18,35].

Practically, the measurement is performed in two steps. First, a spiral flight is performed over the two above-mentioned reference modules. Afterwards, other modules can be evaluated. The soiling loss will be calculated for every image of every cell individually. For each cell, a filtered average is calculated over all images.

A detailed mathematical derivation of the measurement theory can be found in Appendix A.

2.2. Consideration of Electrical Mismatch Effects

The power losses a module experiences due to soiling are denoted SL in this paper. The electrical mismatch losses of a soiled PV module are potentially high and add to the optical losses. A homogeneous soiling leads to a constant shading of a given factor and if all circumstances are the same, the module experiences a reduction in electrical power output very close to this purely optical reduction factor. If, however, the cells are soiled in an inhomogeneous manner, the overall reduction in power output might be higher due to electrical mismatch. Mineral dust is in the beginning rather homogeneously deposited on the module surface. But due to dew, in many cases, dust will accumulate in the lower row of cells of a module leading to an inhomogeneous soiling pattern. Other soiling types like bird droppings are typically inhomogeneous. Figure 1 illustrates the difference between homogeneous and inhomogeneous soiling with mineral dust and bird droppings. The two cases merge into one another. A clear distinction is not always possible. The current voltage curve (IV curve) of each cell is different for this case according to their degree of soiling. The IV curve is an important characteristic of a PV module or cell. The power output is determined by the product of current and voltage. Therefore, the optimal point on the IV curve has to be tracked. A maximum power point (MPP) tracker does exactly this. Such an MPP tracker is either connected to a single module or to a string of modules. The cells are connected in series. Therefore, the same electrical current passes through all cells. This leads to some cells being operated outside of their individual MPP.

Figure 1. Illustrating two different soiling types. Left: two modules next to each other. The left one is soiled with dust and the right one is cleaned. This soiling is classified as homogeneous. The accumulation of dust is slightly stronger only in the lower row of cells. Right: Module soiled with bird droppings. This module is considered to be inhomogeneously soiled.

An electrical model based on the python pvlib by [36,37] has been used to calculate the electrical mismatch losses. It is based on the single diode model. The single diode parameters can be estimated according to the module's data sheet. Every cell is assumed to have the same properties. The electrical model calculates the power output for the clean case and the case of the calculated soiling pattern. By dividing the two powers, we obtain the soiling ratio including mismatch losses. Analysis shows that in all analyzed cases, the soiling was sufficiently small and sufficiently homogeneous so that significant additional

losses due to electrical mismatch can be excluded. The electrical losses of a module are therefore equal to the optical losses arithmetically averaged over all cells for the examples presented in this paper.

3. Data

Three measurement campaigns have been performed in order analyze different soiling conditions. The campaigns took place on 8 April 2022, 8 September 2022, and 25 September 2023 with four, three, and one measurement flights, respectively. The first dataset was recorded to implement the workflow and test the developed methods. Later, more data were recorded for an enlarged validation at different conditions, in particular, with another dust type.

3.1. Measurement Setup

The measurements are performed at CIEMAT's Plataforma Solar de Almería (PSA) on a PV outdoor test bench (PVot, Figure 2). Among other things, the PVot facility is designed for soiling experiments. At the time of the first measurement campaign, there were 12 PV modules, 6 types of modules with 2 modules each. The modules are oriented in the south direction with an elevation angle of 30 degrees. Every module is connected to its own microinverter and MPP tracker. The power of every module is recorded. Furthermore, there are two IV tracers. Additionally, there are reference cells at the test bench to measure the global tilted irradiance (GTI) in the same plane. The electrical soiling losses can be determined by comparing the modules' power outputs to each other or to the GTI as further explained in Section 3.3.2. Less than 10 m away from the test bench is a meteorology station which is equipped with a pyrheliometer whose DNI measurement is used for the evaluations.
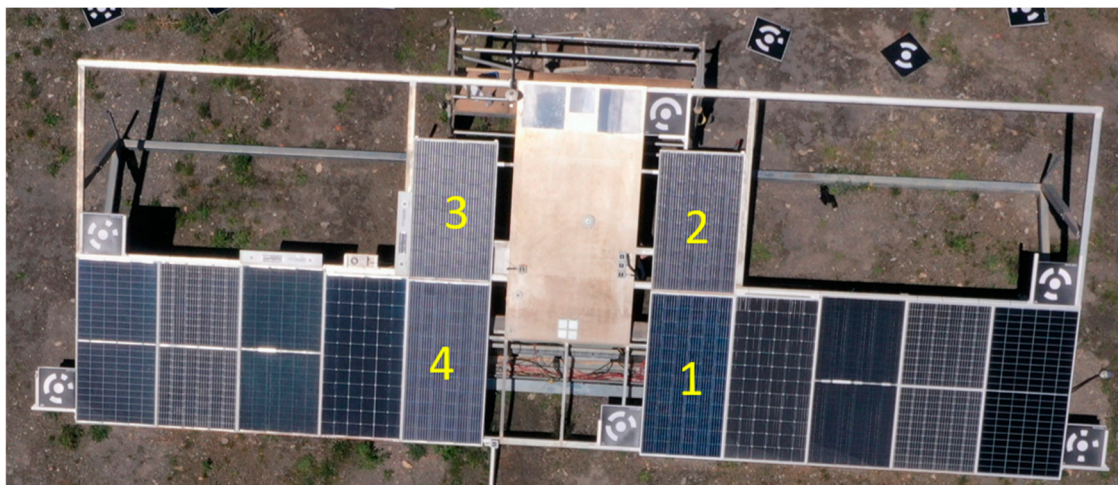

Figure 2. Aerial image of the test bench with 12 modules. Module 1 is clean while the rest were naturally soiled. The central modules numbered 1 to 4 are used for the experiments. The image was taken on the 8 April 2022. At the corners of the setup, one can see the photogrammetry targets that enable the determination of the camera position relative to the modules.

In this measurement campaign, only the four central modules are considered. These are polycrystalline silicon modules manufactured by Axitec. The lower two modules, numbers 1 and 4, consist of 72 cells each while the upper two modules, numbers 2 and 3, have 60 cells each. The nominal powers are 335 W and 280 W. It is assumed that the optical behavior of all cells of the four modules is the same. Module 1 is chosen to be the clean reference module for all campaigns and module 2 is the soiled reference module for the first and the third campaign. In the second campaign, module 4 is chosen as the soiled reference as module 2 was clean then. Note that the modules are typically soiled with local dust. However, on the 8 April 2022, module 4 was soiled with a different type of dust, due

to a sandstorm bringing Saharan dust to Almería. One module was permanently exposed to outdoor conditions after that while the two other modules were stored indoors directly after this dust event until the measurement day to avoid influences from further soiling events and also from natural cleaning. In the third campaign, three modules are soiled artificially with gypsum.

3.2. Measurement Procedure and Data Acquisition

First, the reference measurement is performed. A spiral flight over the clean and the soiled reference module is carried out. Both modules are located directly next to each other so that one flight is sufficient to cover both modules. Afterwards, the measurement flight is performed where the route of the drone is a straight line over the setup in an east–west direction. Figure 3 visualizes the flight route used for the calibration flight. The flight starts in the center, directly above the setup. According to the spiral route, the drone continues to go further to the outside step by step. At the same time, the drone starts at its maximum height and decreases the height the further it goes to the outside of the spiral.
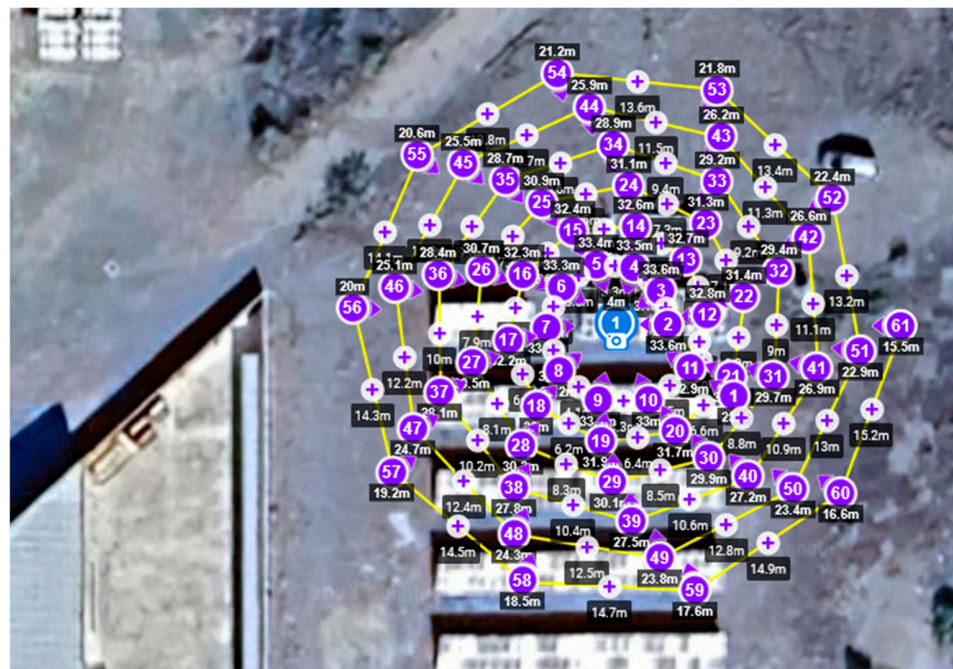

Figure 3. Flight route for the calibration. The points mark the waypoints of the drone. The numbers in the circles indicate the chronological order of the waypoints. The height of the drone for each waypoint is shown in the black boxes.

The electrical power of the four modules, the GTI, and the DNI are recorded permanently. Additionally, for modules 2 and 3, the IV curve is traced. These data are recorded every 10 s. These values are recorded on the measurement day itself and also on a sunny reference day on which all devices are clean. The comparison to this day allows the determination of the reference soiling losses (see Section 3.3.2).

The drone captures both raw images and RGB images. Only the raw images are used for the evaluation. Images are captured every 3 to 5 s. The images contain metadata such as exposure time, aperture, and ISO. For the flight routes used, one pixel in an image corresponds to approximately 6 mm in the module plane in reality.

3.3. Data Processing
3.3.1. Image Processing

Figure 4 visualizes the sequence of the image processing. We use a DJI Mavic 2 Pro (Shenzhen, China) drone for the flights and to capture the images. The images have 5472 by

3648 pixels. The pixel sensors are based on the CMOS technology. The camera has an opening viewing angle of 77 degrees. The evaluation only considers raw images. This ensures that there is a linear relation between irradiance that hits the camera sensor and the values of the corresponding pixels in the image as we also tested using the exposure time series for a constant illumination condition. A camera-specific flat field correction is applied, as mentioned in Appendix A.1. The flat field correction matrix is determined by taking images of an integrating sphere. The integrating sphere has the same brightness at every position. The images of the integrating sphere, however, show a greater brightness in the center. The correction matrix considers the drop of brightness at the images' edges and possible pixel-specific variations in the sensitivity for every pixel (m, n). The dependence of the camera sensitivity on the sensor coordinates can be seen in Equation (1) as the index (m, n) of ε_{mn}. After the flat field correction, this dependence is removed and ε_{mn} simplifies to ε.
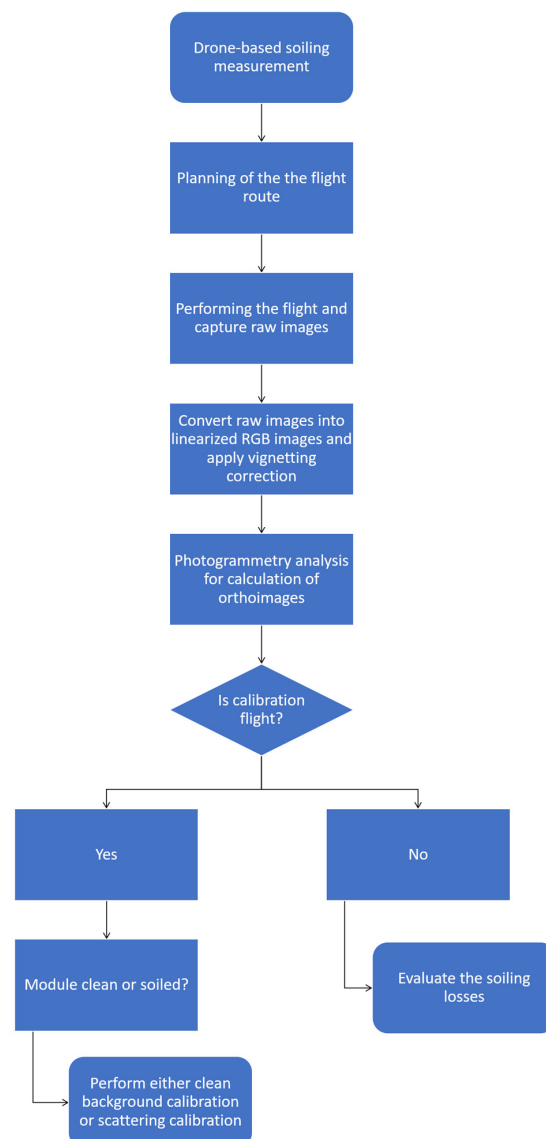

Figure 4. Flow chart of the soiling analysis. The sequence starts with the planning of the flight route. Raw images are then captured. Linearized RGB images with vignetting correction are then calculated. These images are then used for the photogrammetry analysis. As a result, the module can be identified on the images and orthoimages are calculated. In case of a calibration flight, these images are then used for the calculation of the two calibration functions. In case of a measurement flight, the soiling losses are calculated.

Photogrammetry methods are applied to calculate rectified orthographic images as described in detail in [38]. Input is in particular a coordinate system defined by the photogrammetry target in the corners of the setup seen in Figure 2. Also, the position of each module within this coordinate system is given as an input. The photogrammetry can then calculate the camera position relative to each module for each image. The so-called orthoimages of each module are cut into individual cells. This is performed by applying a mask that aligns with the modules' edges. The position of each module is given in a reference coordinate system which allows the distinction of all modules. For each orthoimage, the sun position is calculated from the timestamp. The camera position relative to the cell is calculated. This information is sufficient to describe the geometry. The brightness of each cell of each orthoimage is extracted and normalized to the GTI at a certain timestamp.

Afterwards, the calibrations and the evaluation are performed in the following order. First, the clean reference module is analyzed (see the method from Appendix A.2.1) followed by the soiled reference module (Appendix A.2.2). Afterwards, it is possible to analyze all other modules (Appendix A.2.3). For every image of a given cell a soiling loss is calculated. The final soiling value of a cell is the filtered average over all images to exclude outliers (see Appendix A.2.3).

3.3.2. Calculation of Electrical Losses for Calibration of c_{scat} and Validation

There are two ways that are used to electrically determine the soiling losses SL_{ref} of the modules for the calibration and validation in this work. In the first and more accurate way, the power of the soiled module is compared to the power of the clean module. Additionally, a normalization factor has to be applied which considers that the modules have different nominal powers and have aged differently. Therefore, the ratio of powers is normalized by its value when both modules are clean [16].

Alternatively, the power of the soiled module can also be compared to its expected power in the clean state calculated using reference cell data [35]. On a day where both the reference cell and the module are clean, the ratio between module power and the reference cells PV-matched and temperature-corrected GTI is calculated in a symmetrical time window of one hour around solar noon. The same ratio is determined for the measurement day where the module is soiled and the reference cell continues to be clean. By dividing both ratios, and applying a temperature correction for the module power, the soiling ratio is obtained. The PV module temperature has to be considered as the module temperature increases as its efficiency decreases. For normal operating temperatures, a linear dependence between the module temperature and efficiency is valid. The manufacturer states the temperature coefficient in the data sheet, -0.4% per K temperature increase. The module temperature is measured with a Pt-100 and the module power will be temperature-corrected to an arbitrarily chosen reference temperature of $40\,^{\circ}\mathrm{C}$ for every timestamp. The corrected power is calculated by considering the measured deviation from the reference temperature and multiplying the temperature difference with the temperature coefficient from the data sheet. In the case of determining the soiling loss by comparing the soiled modules' powers to the clean module's power, a temperature correction is not necessary because it is assumed that the clean and the soiled module have a very similar temperature and their efficiencies are assumed to have the same temperature dependence. This way it is indifferent if the modules have a different temperature on the measurement day and the reference day. As mentioned above, the reference cell data are also temperature corrected. The short circuit current increases with the temperature. In case of the used module, the coefficient of the short circuit current increase is 0.04% per Kelvin.

For the first campaign, the soiling losses are determined by comparing to the reference cell as the power of the clean module was then not recorded continuously. For the following campaigns, the soiling is determined via the module-to-module comparison method.

For all electrical measurements, data of up to one hour around solar noon are considered. This is a tradeoff between achieving better statistics because of a large number

of data points and at the same time ensuring that only low incidence angles are used. In the morning and in the evening, the sunlight falls on the module at a high incidence angle. This changes the soiling loss as the soiling layer appears thicker for higher incidence angles. Additionally, small misalignments of the module planes, which are negligible for nearly normal incidence, typically show a higher impact in the morning and evening hours. It has been found that the module and the reference cell are sufficiently in plane so that a correction for the incidence angle is not necessary when analyzing only data close to solar noon.

Note that the electrically measured reference soiling loss is an input for the presented optical method. Therefore, the accuracy of the optical method is limited by the accuracy of the electrical reference measurement. This is also true for the AI methods mentioned in the introduction by Mehta et al. [33] and by Yang et al. [34] and will be true for any optical method that requires a calibration with electrical reference measurements.

A few days after each campaign, all modules are cleaned to perform the above-mentioned normalization. Appendix B.2 shows the calculation of the electrical reference loss for all modules and test days.

4. Results and Discussion

All flights performed on the three days are evaluated. As an example, the results of the first flight of the first campaign are shown here in detail, while the other two days are presented in Appendix B. Figure 5 shows the cell-resolved soiling of all four modules that were calculated for the given flight. The lower right module was used as the clean reference module and the upper right module was used as the soiled reference module.
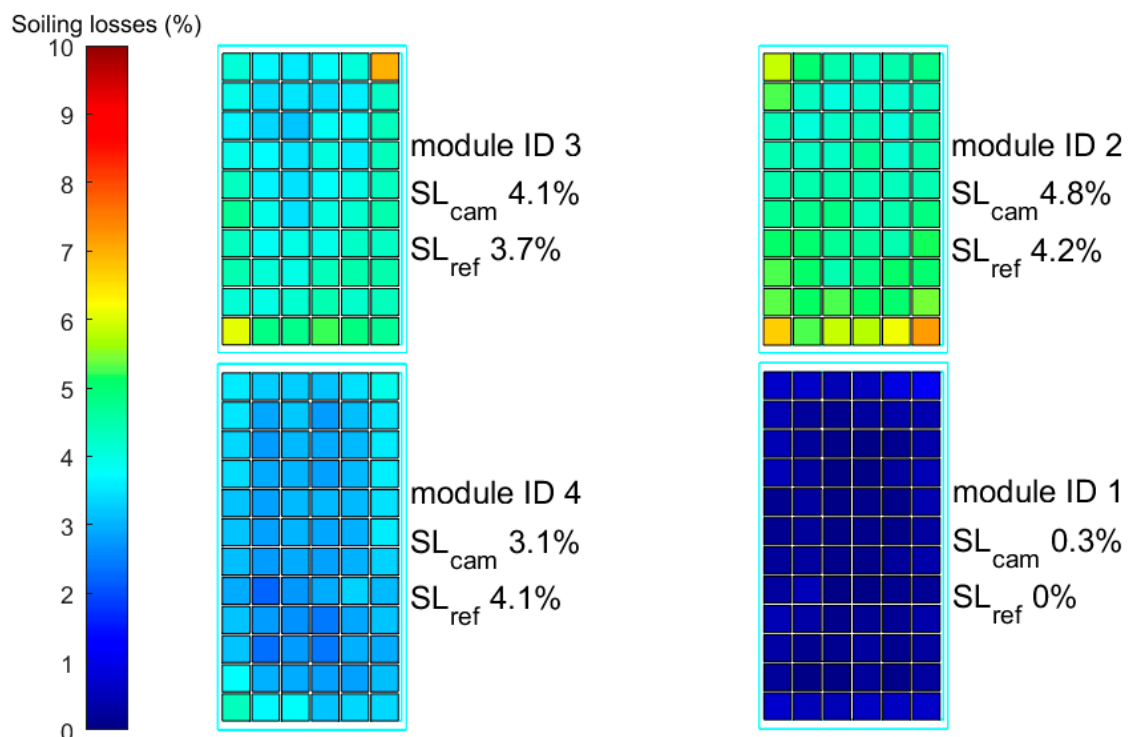

Figure 5. Results of the first flight performed on the 8 April 2022. The color marks the calculated soiling loss. The lower right module (1) was used as the clean calibration module while the upper right (2) was used as soiled reference module. The upper numbers label the modules. The number in the middle states the optically measured soiling loss using the drone images while the lower number is the electrical reference loss.

Figure 6 shows the optically measured soiling loss against the electrically measured reference soiling loss for every image. In contrast to Figure 5, the optically measured soiling

loss SL_{cam} in Figure 6 is module resolved and not cell resolved and is not yet averaged over all images. As can be seen, the calculated module soiling loss is similar for every image and there are no major outliers.
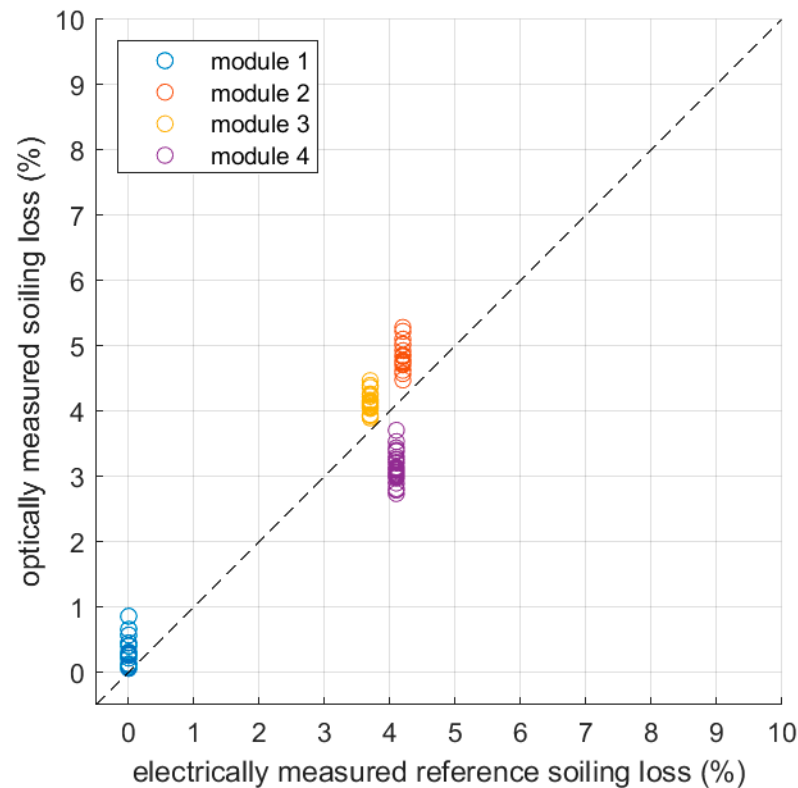

Figure 6. Optically calculated soiling loss for every image of every module against the electrically measured reference soiling loss. The standard deviations for the soiling loss on module level for modules 1 to 4 are 0.14%, 0.22%, 0.20%, and 0.18%, respectively. The results belong to the first flight performed on 8 April 2022.

According to the results, the soiling distribution of each module seems to be roughly homogeneous. However, there are a few cells that have a different soiling loss than their neighboring cells. In particular, the lower right cell of module 2 and the upper right cell of module 3 have a higher soiling loss. This observation in the results corresponds to the expectation from the photo shown in Figure 7. One can clearly see that the upper right cell of the upper left module is brighter and more soiled than its neighbors. The same applies for the lower right cell of the upper right module.

The calculated soiling loss of the clean module is 0.3% and the soiling loss of the soiled reference module is 4.8%. These values differ slightly from the electrical reference values that were used to calibrate the method (0% and 4.2%, respectively). These differences are explained by the fact that the results shown here were created by evaluating different images from different perspectives compared to the calibration. The calculated soiling loss for the upper left module is 4.1% which is close to the electrically measured reference value of 3.7%. The measured value of the lower left module is 3.1% and differs more from the electrical reference value of 4.1%. This might be explained by the fact that the upper modules were soiled with a different soiling type compared to the lower left module.

As mentioned above, the detailed analyses of the other measurement flights of the first campaign and the analyses of the other campaigns can be found in Appendix B.
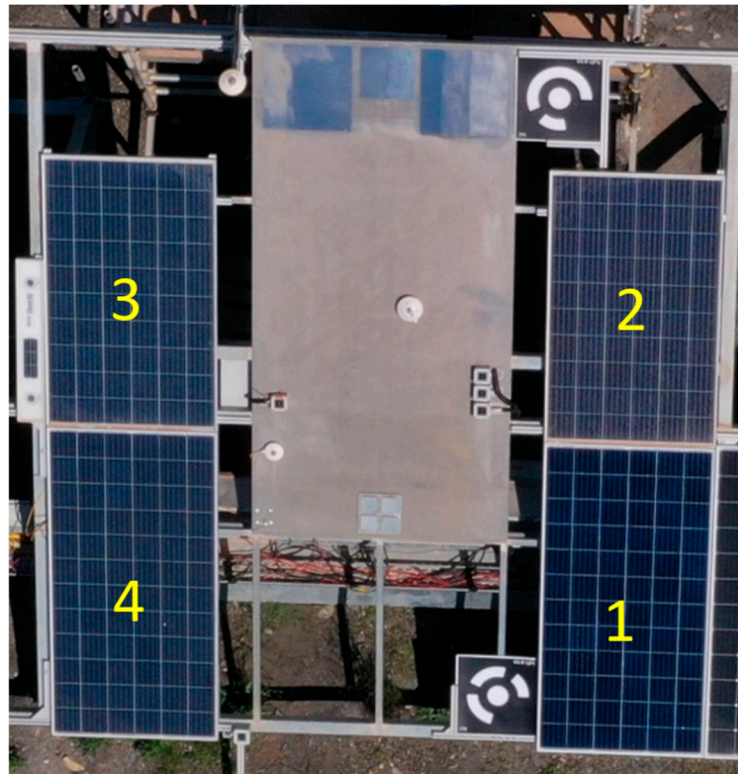
Figure 7. Image of the soiled setup. The module on the lower right was used for the clean calibration while the upper right module was used as the soiled reference module. Both modules on the left were used for validation of the method.

Figure 8 summarizes the results of all measurements performed. It shows the optically measured soiling losses against the electrically measured reference soiling losses. The values are presented on a module level. The RMSE of the measured soiling loss over all measurements is 0.93% absolute. The MAE is 0.70% absolute and the MBE is 0.33% absolute. These three metrics are defined in Equations (1)–(3). With N being the total number of data points, i identifies each individual data point, x_i is the optically measured value, and $\hat{x}_i$ is the electrically measured reference value.

$$RMSE = \sqrt{\frac{\sum_{i=1}^{N}(x_i - \hat{x}_i)^2}{N}} \tag{1}$$

$$MAE = \frac{\sum_{i=1}^{N}|x_i - \hat{x}_i|}{N} \tag{2}$$

$$MBE = \frac{\sum_{i=1}^{N}(x_i - \hat{x}_i)}{N} \tag{3}$$

The red dot refers to the above-discussed measurement for which the test and soiled reference modules had a different soiling type. This different soiling type explains the higher deviations. The blue triangle and the dark red rhombus refer to the third measurement campaign where the modules were soiled artificially with gypsum. The artificial soiling is not as homogeneous as the natural soiling. Hence, the approximation for the calibration that all cells of the soiled reference module have the same soiling level is less adequate and higher deviations can be explained.

One can see that in some cases the method overestimates and in other cases it underestimates the soiling losses. According to [39,40], the uncertainty of the electrical measurements of the soiling loss is about 1% absolute. This is the same magnitude as the calculated RMSE. There are not yet enough data to state whether the bias error of the method is systematic

or not. The method is qualitatively able to distinguish between stronger and less soiled modules and also stronger and less soiled cells. Additionally, it can give a reasonable estimation of the absolute soiling value.
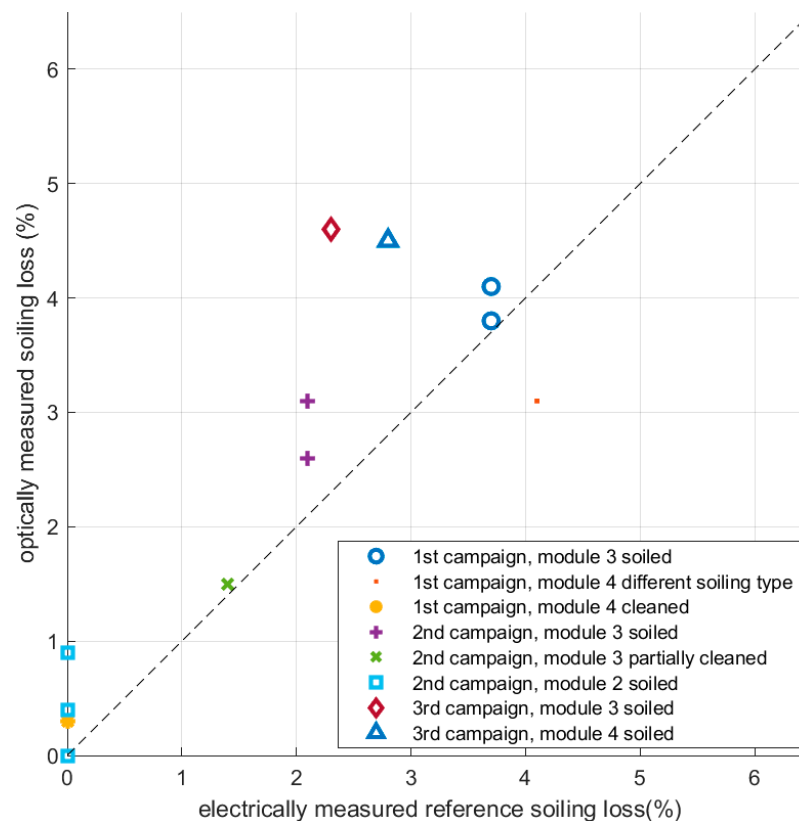

Figure 8. Optically measured soiling losses based on the images plotted against the electrically measured reference soiling losses for several modules and the three measurement campaigns performed. For some campaigns and modules, several identical markers are seen referring to different flights within the same campaign.

There is no obvious benchmark model that could be compared with the proposed model because of its novelties. The most similar model is probably the AI model by Yang [34] that calculates the soiling losses from just seeing an image. The authors state that the relative prediction error is below 10% if the actual soiling loss exceeds 8% absolute. According to Figure 4 of their paper, this is the case in a minority of the cases. Unfortunately, the average soiling loss, the RMSE, the MBE, and the MAE are not stated. Figure 4 of the Yang paper is similar to Figure 8 here. Yang has analyzed a wider range of soiling losses. In the range up to 8% absolute soiling loss, the deviation between the measurement and the prediction seem to be comparable to the proposed method. When making this comparison, one has to be extremely careful and has to keep in mind that both models were tested on different datasets. Yang et al. used the same camera and the same perspectives for all images. Additionally, the same modules were used for training and evaluation. All in all, both methods should be tested under various conditions to allow a fair comparison.

5. Conclusions

This paper presents a new method to optically measure the soiling loss of PV modules soiled with dust with a high spatial resolution. The method is capable to properly estimate the soiling losses, with an RMSE of 0.93% absolute in the validations. Individual cells with a higher soiling can be identified. Also, on the module level, a qualitative distinction between more and less soiled modules is possible.

The method's calibration requires two reference measurements of a clean and a soiled module. The calibration is performed before every individual measurement. The brightnesses of the clean module are extracted from various perspectives and this is also performed for the soiled reference module for which the soiling losses are also determined electrically. The soiled module is typically brighter as there is more light scattering at the module's surface. Conclusions about the scattering behavior of the dust on top of the module are drawn from the images. After understanding this behavior, it is possible to evaluate other modules.

As the method is based on analyzing drone images, it could be applied to a larger scale and could potentially cover entire PV plants. Currently, the method calculates the soiling loss on a cell level, which allows the consideration of mismatch effects within the modules. When modules are connected in a series in bigger parks, there are additional mismatch losses from module to module. These losses can also be considered when knowing the soiling loss with a spatially high resolution. A combination of this method with thermography measurements enables the distinction of soiling-based and defect-based hotspots.

Near-future plans consist of testing the method on a larger scale. In parallel to this work, another algorithm was developed to also detect other kinds of soiling beyond dust. These might be inhomogeneous soiling like bird droppings, leaves, or snow. The two methods are foreseen to be combined in the near future. Simplifying the method's calibration is also a goal. Additionally, it is planned to further investigate the properties of the calibration function. For example, it might be possible to create a calibration that can be performed once and does not have to be repeated for every measurement campaign. This could enhance the practicability of the method as there would no longer be the need for measuring the individual power of one homogeneously soiled module.

Author Contributions: Conceptualization, P.W. and S.W.; methodology, P.W., F.W. and S.W.; software, P.W. and J.J.K.; validation, P.W. and B.N.; formal analysis, P.W. and S.W.; data curation and data acquisition, N.A. and P.W; writing—original draft preparation, P.W.; writing—review and editing, all authors; visualization, P.W.; supervision, S.W., R.P.-P., M.R., M.C.A.-G., J.P. and A.F.-G.; project administration, S.W.; funding acquisition, S.W. All authors have read and agreed to the published version of the manuscript.

Data Availability Statement: Data are available upon reasonable request.

Conflicts of Interest: Marc Röger, Fabian Wolfertstetter and Stefan Wilbert hold the following patent DE 10 2017 211 466 B3 that is related to the publication. Peter Winkel, Stefan Wilbert and Fabian Wolfertstetter applied for another patent (PCT/EP2024/067239) that is related to the publication. The methods described in the patents can be used to measure PV soiling losses. Dr. Wolfertstetter contributed to the publication while working at DLR and currently works in the company Volateq GmbH. The companies commercializes drone-based PV soiling measurements. The authors declare no conflict of interest.

Appendix A

Appendix A.1. Optical Measurement Theory

Figure A1 illustrates the geometry of the measurement. For the diffuse radiation, only one beam is sketched exemplary, while diffuse radiation is coming from the entire hemisphere. The reflected and scattered light is indicated with an ellipse because light scattering takes place in various directions. It has to be noted that the sun vector, the module normal vector, and the camera vector (drone vector) do not have to be in plane

in the three-dimensional case. This is a simplification for the illustration. All vectors are pointing away from the module.
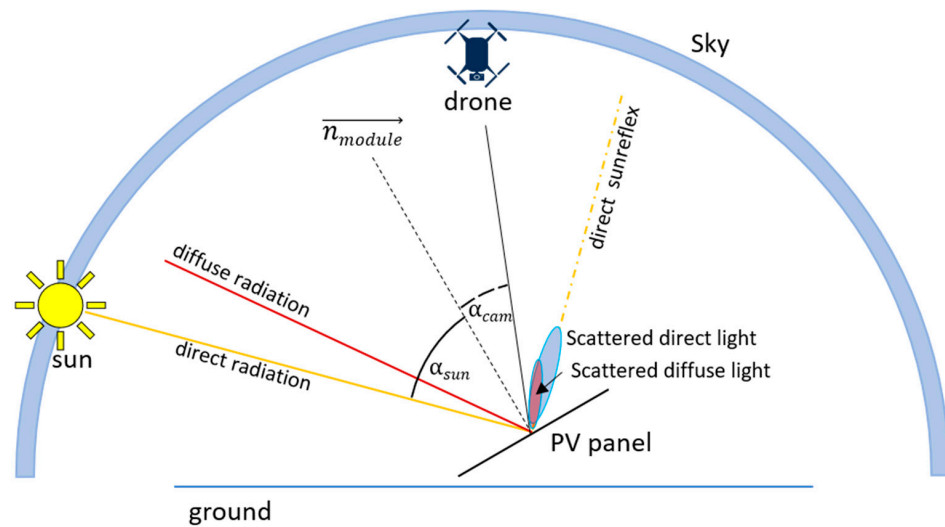

Figure A1. Sketch to describe the geometry of the measurement method. Shown are the sun position, a direct sun ray towards the PV module, the drone position, and the module position including its normal vector $\overrightarrow{n_{module}}$. Also, one exemplary ray contributing to the diffuse radiation received that is received by the module is shown. Additionally, the direct sun reflex is shown together with the reflex of the diffuse radiation of one exemplary point in the sky.

Appendix A.1.1. Relation of the RGB Values to the Incoming Radiation

The camera mounted on the drone is used as a sensor. The captured images are interpreted as irradiance maps. Each pixel corresponds to a certain irradiance caused by radiation coming from a certain direction. The relation between the irradiance and the pixel's RGB values is described by the camera equation (Equation (1)) [41,42].

$$\overrightarrow{RGB_{mn}} = \Gamma_{RGB}\left(\overline{\overline{M_{cam}}} \cdot \int_{A_{mn}} \int_{\lambda_{min}}^{\lambda_{max}} t_{exp} \cdot \overrightarrow{\varepsilon_{mn}} \cdot E_\lambda\left(\overrightarrow{r_{cam}}, \overrightarrow{x_{obj}}, t_{acqui}\right) dA d\lambda\right) \quad \text{(A1)}$$

$\overrightarrow{r_{cam}}$ is the vector from the object seen in pixel (m, n) to the entrance pupil of the camera. $\overrightarrow{x_{obj}}$ is the position of the object seen in pixel (m, n) in a global coordinate system. $\overrightarrow{RGB_{mn}}$ is a vector containing the three-color channel values of a certain pixel (m, n). Γ_{RGB} is the camera-specific gamma correction that considers the potentially non-linear response in terms of irradiance. $\overline{\overline{M_{cam}}}$ is the camera-specific color-mixing matrix, A_{mn} is the pixel area of the pixel, $\overrightarrow{\varepsilon_{mn}}$ is its color channel-dependent spectral responsivity, and λ_{min} and λ_{max} are the minimum and the maximum wavelengths of the spectrum that are detected by the camera. The exposure time of an image is denoted t_{exp}. E_λ is the wavelength-dependent irradiance that is caused by radiation reaching the camera at the time of the image acquisition t_{acqui} from the specific perspective and object.

Assuming that $\overrightarrow{\varepsilon_{mn}}$ and E_λ are constant over the pixel's area, we solve the integral over the pixel area. We also assume that the pixel area is independent of the sensor coordinates (m, n) so that it is simplified to A. In the following, only the red color channel is considered, and it is assumed that the matrix elements of $\overline{\overline{M_{cam}}}$ on the main diagonal are dominant. Accordingly, $\overrightarrow{\varepsilon_{mn}}$, $\overline{\overline{M_{cam}}}$, and the vector $\overrightarrow{RGB_{mn}}$ simplify to ε_{mn}, m_{cam}, and R_{mn}. Additionally, the gamma correction can be neglected when considering only linearized images. Furthermore, the variation in the camera's sensitivity ε_{mn} with the sensor coordinates (m, n) can be removed from using a flat field correction. This will be

considered before using the images for any evaluations and is described in more detail in Section 3.3. Hence, ε_{mn} simplifies to ε. Accordingly, R_{mn} is not explicitly dependent on (m, n) anymore, which is why the index will be neglected from now on. The variation in R can be expressed using the arguments $(\overrightarrow{r_{cam}}, \overrightarrow{x_{obj}}, t_{acqui}, t_{exp})$, if all camera settings except the exposure time are fixed.

$$R(\overrightarrow{r_{cam}}, \overrightarrow{x_{obj}}, t_{acqui}, t_{exp}) = m_{cam} \cdot A \cdot t_{exp} \int_{\lambda_{min}}^{\lambda_{max}} \varepsilon \cdot E_\lambda \left(\overrightarrow{r_{cam}}, \overrightarrow{x_{obj}}, t_{acqui} \right) d\lambda \qquad \text{(A2)}$$

This relation between the irradiance caused by the radiation received from a certain object element and the red channel in the corresponding image element will be used to connect the brightness increase to the incoming solar irradiance and the soiling loss in the following.

Appendix A.1.2. Contributions to the Camera Signal According to the Interaction at the Module's Surface

We first consider an image of a soiled module. The irradiance E_λ^{soiled} which falls from the soiled module into the camera can be split into different terms. The subscript λ indicates the wavelength dependence of the irradiance. The superscript "soiled" indicates that the irradiance is coming from a soiled module. The first contribution is $E_{\lambda,scat,dir}^{soiled}$ which denotes the direct irradiance scattered at the soiling layer of the module that hits the camera. On the other hand, there is $E_{\lambda,refl}^{soiled}$ that describes the reflected irradiance at the module's surface that is hitting the pixel. It consists of both direct and diffuse irradiance and it considers both specular and diffuse reflection. There is also scattering of the diffuse irradiance towards the camera, but this term is neglected because the scattered direct irradiance is much greater than the diffuse irradiance for sunny conditions. We ensure that this assumption is correct by requiring that the modules are not shaded by clouds during the measurements and by limiting the evaluation to small incidence angles of the direct irradiance (less than $40°$).

$$E_\lambda^{soiled} = E_{\lambda,scat,dir}^{soiled} + E_{\lambda,refl}^{soiled} \qquad \text{(A3)}$$

In case of a clean module, indicated by the superscript "clean", the equation simplifies as follows.

$$E_\lambda^{clean} = E_{\lambda,refl}^{clean} \qquad \text{(A4)}$$

We will show in the following how $E_{\lambda,refl}^{clean}$ and $E_{\lambda,refl}^{soiled}$ are related to each other.

Appendix A.1.3. Comparing the Camera Equation for the Clean and Soiled Case

The measurement equation is derived by comparing the camera equation for the clean and soiled cases of Equation (A2).

$$R_{clean/soiled} = m_{cam} \cdot A \cdot t_{exp} \int_{\lambda_{min}}^{\lambda_{max}} \varepsilon \cdot E_\lambda^{clean/soiled} (\overrightarrow{r_{cam}}, \overrightarrow{x_{obj}}, t_{clean/soiled}) d\lambda \qquad \text{(A5)}$$

The point in time when the image of the soiled module is captured is denoted t_{soiled} and t_{clean} is the acquisition time of the image of the clean module.

These equations can be simplified further by dividing by the constants and the known exposure time so that these parameters and the red pixel value are combined in one parameter, respectively $R_{soiled,exp.norm}$ or $R_{clean,exp.norm}$. This results in the following:

$$R_{clean/soiled,exp,norm} = \int_{\lambda_{min}}^{\lambda_{max}} \varepsilon \cdot E_\lambda^{clean/soiled} (\overrightarrow{r_{cam}}, \overrightarrow{x_{obj}}, t_{clean/soiled}) d\lambda \qquad \text{(A6)}$$

With

$$R_{clean/soiled,exp,norm} = \frac{R_{clean/soiled}}{m_{cam} \cdot A \cdot t_{exp}} \tag{A7}$$

E_λ^{clean} can be written as shown in Equation (3) and simplified using a hereby defined function $c_{refl}(\overrightarrow{r_{cam}}, \overrightarrow{r_{sun}})$:

$$R_{clean,exp,norm}(\overrightarrow{r_{cam}}, \overrightarrow{x_{obj}}, t_{clean}) = \int_{\lambda_{min}}^{\lambda_{max}} \varepsilon \cdot E_{\lambda,scat,dir}^{clean}(\overrightarrow{r_{cam}}, \overrightarrow{x_{obj}}, t_{clean})$$
$$d\lambda = c_{refl}(\overrightarrow{r_{cam}}, \overrightarrow{r_{sun}}) \cdot GTI(t_{clean}) \tag{A8}$$

On the one hand, R_{cl} is proportional to the illumination of the module, described by the global tilted irradiance $GTI(t_{clean})$ in the plane of the module at the point in time t_{clean} of capturing the image of the clean module. On the other hand, it is assumed that all dependencies of the geometry can be summarized in a function $c_{refl}(\overrightarrow{r_{cam}}, \overrightarrow{r_{sun}})$. It is assumed that all cells show the same optical behavior in the clean state so that at the end, R_{cl} does not depend on $\overrightarrow{x_{obj}}$ anymore. This assumption is acceptable for many PV modules, but there are also PV modules for which it is not applicable. If different cells, e.g., within a polycrystalline PV module, look noticeably different, the method will hence most likely lead to higher deviations. Furthermore, it is assumed that the optical properties of the cells are described well by a rotational symmetry for c_{refl} around the module normal vector $\overrightarrow{n_{module}}$. Correspondingly, c_{refl} can also be described by a set of three angles: the angle between the camera vector and the normal vector α_{cam}, the angle between the sun vector $\overrightarrow{r_{sun}}$ and the normal vector α_{sun}, and the angle between the camera vector and the sun vector $\theta_{cam,sun}$. There are also other combinations of angles that can describe the situation. For example, the angle $\theta_{cam,reflexsun}$ between the camera and the sun reflex vector $\overrightarrow{r_{sunreflex}}$ might be suited better than the angle $\theta_{cam,sun}$ between the camera vector and the sun vector.

For the case of a soiled module, we can use Equation (A1) and $c_{refl}(\overrightarrow{r_{cam}}, \overrightarrow{r_{sun}})$ as explained in the following to obtain Equation (A6).

$$R_{soiled,exp.norm}(\overrightarrow{r_{cam}}, \overrightarrow{x_{obj}}, t_{soiled})$$
$$= \int_{\lambda_{min}}^{\lambda_{max}} \varepsilon \cdot E_{\lambda,scat,dir}^{soiled}(\overrightarrow{r_{cam}}, \overrightarrow{x_{obj}}, t_{soiled})d\lambda$$
$$+ \int_{\lambda_{min}}^{\lambda_{max}} \varepsilon \cdot E_{\lambda,refl}^{soiled}(\overrightarrow{r_{cam}}, \overrightarrow{x_{obj}}, t_{soiled})d\lambda \tag{A9}$$
$$= R_{scat}(\overrightarrow{r_{cam}}, \overrightarrow{x_{obj}}, t_{soiled}) + c_{refl}(\overrightarrow{r_{cam}}, \overrightarrow{r_{sun}}) \cdot \tau(\alpha_{sun}) \cdot \tau(\alpha_{cam}) \cdot GTI(t_{soiled})$$

R_{soiled} consists of two parts. R_{scat} is defined as the contribution related to the first integral and corresponds to the scattering at soiling particles. The second summand in the equation is similar to Equation (A5) for the clean module and can be interpreted as the brightness without scattering by soiling particles—or in other words, basically, roughly the brightness one would see if the module was clean. The factors $\tau(\alpha_{sun})$ and $\tau(\alpha_{cam})$ consider that the reflection signal is attenuated compared to the clean case. τ is the wavelength-averaged transmittance of the soiling layer. It depends on the angle under which the radiation falls on the soiling layer, so that two typically different transmittances appear in the equation. The soiling layer is passed by the reflected light first under the angle α_{sun} and afterwards under the angle α_{cam}. Under the above assumptions for the properties of the cells, $c_{refl}(\overrightarrow{r_{cam}}, \overrightarrow{r_{sun}})$ is the same for the clean module and the soiled module, as long as the geometry defined by $\overrightarrow{r_{cam}}$ and $\overrightarrow{r_{sun}}$ is the same.

Equations (A5) and (A6) are then connected to each other—we try to rewrite Equation (A6) using $R_{clean,exp,norm}$ from Equation (A5). For this, we consider images of a clean module element and a soiled module element taken from the same relative position of the camera to the module element $\overrightarrow{r_{cam}}$ and $\overrightarrow{r_{sun}}$. Then, we solve Equation (A5) for

$c_{refl}(\overrightarrow{r_{cam}}, \overrightarrow{r_{sun}})$ and substitute the result in Equation (A6). In doing so, we assume that the transmittances did not change between the two image acquisitions. The resulting equation links the clean and the soiling images and is the basis for deriving the soiling loss.

$$
\begin{aligned}
R_{soiled,exp,norm}&(\overrightarrow{r_{cam}}, \overrightarrow{x_{obj}}, t_{soiled}) \\
&= R_{scat}(\overrightarrow{r_{cam}}, \overrightarrow{x_{obj}}, t_{soiled}) + R_{clean,exp,norm}(\overrightarrow{r_{cam}}, \overrightarrow{x_{obj}}, t_{clean}) \\
&\cdot \tau(\alpha_{sun}) \cdot \tau(\alpha_{cam}) \cdot \frac{GTI(t_{soiled})}{GTI(t_{clean})}
\end{aligned}
\tag{A10}
$$

The equation also considers that the clean and soiled images might have been taken at different times with different illumination situations. This is included in the equation by the ratio of the global tilted irradiances at the time of the respective image acquisition ($GTI(t_{soiled})$, $GTI(t_{clean})$). Equation (A7) can be reformulated to Equation (A8) which more clearly describes the transmittance of the soiling layer.

$$
\tau(\alpha_{sun}) \cdot \tau(\alpha_{cam}) = \frac{R_{soiled,exp,norm} - R_{scat}}{R_{clean,exp,norm}} \cdot \frac{GTI(t_{clean})}{GTI(t_{soiled})}
\tag{A11}
$$

In this equation, τ has to be calculated. The transmission $\tau(\alpha)$ of the soiling layer depends on the angle of incidence α. For normal incidence, the value of τ reaches its maximum τ_0. For an oblique incidence, the soiling layer effectively appears thicker and the soiling losses will increase. In this work, it is assumed that the transmittance is described by the effective thickness of the soiling layer as in Equation (A9). All viewing angles and incident angle are limited to small values so that this assumption is expected to hold.

$$
\begin{aligned}
1 - \tau(\alpha) &= \frac{1-\tau_0}{\cos \alpha} \cdot \\
\tau(\alpha) &= 1 - \frac{1-\tau_0}{\cos \alpha}
\end{aligned}
\tag{A12}
$$

There are more complex models in literature to describe the angular dependence of the soiling on reflecting mirrors, e.g., [43], but we use the described approach for simplicity. With this assumption, the left side of Equation (A8) only contains the cosines of the two known angles and the parameter that we want to determine, the transmittance τ_0.

The parameters on the right side of Equation (A8) are partly known. $R_{soiled,exp.norm}$ is proportional to the red channel of the soiled module's image and $R_{clean,exp,norm}$ to that of the clean reference module. $R_{soiled,exp,norm}$ and $R_{clean,exp,norm}$ have to be compared for the same geometry described by the sun position $\overrightarrow{r_{sun}}$ and $\overrightarrow{r_{cam}}$ the camera's position relative to the PV cell. Of particular interest is the orientation of $\overrightarrow{r_{sun}}$ and $\overrightarrow{r_{cam}}$ to each other. For instance, the most important aspect is how close the camera viewing point is to the direct sun reflex as this might cause over-exposure and direct reflexes. The GTIs are measured and known. R_{scat} is unknown for the moment and will be further discussed in Appendix A.1.4. It depends on the properties of the soiling layer including its transmittance τ and the illumination and viewing geometry. It should be mentioned that $R_{soiled,exp,norm}$, R_{scat}, and $R_{clean,exp,norm}$ depend on $\overrightarrow{r_{cam}}$, $\overrightarrow{r_{sun}}$, and on $GTI(t_{acqui})$. $R_{soiled,exp,norm}$ and R_{scat}, additionally, depend on the local soiling $\tau_0(\overrightarrow{x_{obj}})$. In the following, it is assumed that $\tau_0(\overrightarrow{x_{obj}})$ is an average over the area of each cell.

Equation (A8) can be simplified further by normalizing to the *GTIs*.

$$
\tau(\alpha_{sun}) \cdot \tau(\alpha_{cam}) = \frac{R_{soiled,GTI,norm} - R_{scat}/GTI(t_{soiled})}{R_{clean,GTI,norm}}
\tag{A13}
$$

with

$$R_{clean/soiled,GTI,norm} = \frac{R_{clean/soiled,exp,norm}}{GTI(t_{clean/soiled})} \tag{A14}$$

Appendix A.1.4. Analyze Different Scattering Pathways

To further understand Equation (A10) and R_{scat}, we analyze the underlying scattering pathways. There are multiple scattering pathways possible even if only first-order scattering is considered. The scattering pathways are sketched in Figure A2. It can be shown by geometrical considerations that the scattering angles are the same for the cases I, I and II, II as well as for I, II and II, I, respectively. The angles are explained in Tables A1 and A2.
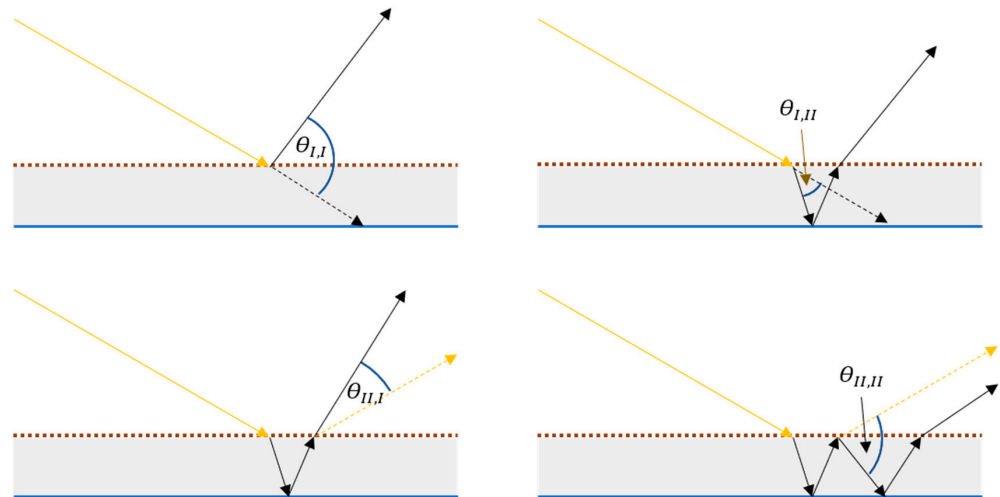
Figure A2. Sketch to describe the scattering pathways relevant for the measurement method. The cover glass is shown as a grey surface with the soiling layer on top (dotted brown line) and the PV cell below (straight blue line). Shown is the direct radiation coming from the sun as a straight yellow arrow. The black arrow with a straight line shows in which direction the light leaves if it is scattered (camera direction). The dashed yellow or black arrows show the direction relative to which the scattering angle is defined. In the lower two subfigures, the yellow dashed arrow corresponds to the direct sun reflex.

Table A1. Explanation of the different scattering angles and pathways.

Nomenclature	Case Description
I, I	The incident irradiance is scattered in the direction of the camera without interacting with the glass cover.
I, II	The incident irradiance is scattered in the direction of the module. Then, it is refracted at the air–glass surface. Afterward, the light is reflected at the cell's surface. Then, it is refracted at the glass–air surface. When leaving in the direction of the camera, the irradiance is transmitted through the soiling layer.
II, I	The incident irradiance is transmitted through the soiling layer. Then, it is refracted at the air–glass surface. At the cell's surface, the irradiance is reflected. Then, it is refracted at the glass–air surface. When leaving the module, the irradiance is scattered in the direction of the camera.
II, II	The incident irradiance is transmitted through the soiling layer. Then, it is refracted at the air–glass surface. When reaching the cell's surface, the irradiance is reflected. Then, it is refracted at the glass–air surface. When reaching the soiling layer for the second time, the light is scattered in the direction of the cell. Then, it is again refracted at the air–glass surface. Afterwards, the light is reflected by the cell surface for a second time. Then, it is refracted at the glass–air surface Finally, it is transmitted through the soiling layer in the direction of the camera.

Table A2. Comparison of the different scattering angles.

Nomenclature	Case Description
$\theta_{I,I}(\overrightarrow{r_{cam}}, \overrightarrow{r_{sun}}) = \theta_{II,II}(\overrightarrow{r_{cam}}, \overrightarrow{r_{sun}})$	Angle between camera vector and sun vector; the camera vector is pointing in the direction of the module and the sun vector is pointing away from the module.
$\theta_{I,II}(\overrightarrow{r_{cam}}, \overrightarrow{r_{sun}}) = \theta_{II,I}(\overrightarrow{r_{cam}}, \overrightarrow{r_{sun}})$	Angle between the sun reflex vector and the camera vector; both vectors are pointing away from the module.

Considering the four pathways, we now formulate an equation describing $L_{\lambda,scat,dir}$, which is the wavelength-dependent radiance of the direct radiation that is scattered once by the soiling particles and reaches the sensor.

$$
\begin{aligned}
L_{\lambda,scat,dir}^{soiled}(\overrightarrow{r_{cam}}, \overrightarrow{r_{sun}}) \\
= L_{\lambda,dir}^{soiled}(\overrightarrow{r_{sun}}) \cdot \omega \\
\cdot [(1 - \tau(\alpha_{sun})) \cdot P_{scat}(\theta_{I,I}, \lambda) + (1 - \tau(\alpha_{cam})) \cdot \tau(\alpha_{sun}) \\
\cdot \rho_{spec} \cdot P_{scat}(\theta_{I,II}, \lambda) + (1 - \tau(\alpha_{sun})) \cdot \tau(\alpha_{cam}) \cdot \rho_{spec} \\
\cdot P_{scat}(\theta_{II,I}, \lambda) + (1 - \tau(\alpha_{cam})) \cdot \tau(\alpha_{sun}) \cdot \tau(\alpha_{cam}) \cdot \rho_{spec}^2 \\
\cdot P_{scat}(\theta_{II,II}, \lambda)]
\end{aligned} \tag{A15}
$$

$L_{\lambda,dir}^{soiled}$ is the wavelength-dependent direct radiance falling on the soiled module. ω is the single scattering albedo, i.e., the ratio of the particles' scattering coefficient to their extinction coefficient. ω describes that only a fraction of the radiation that is not transmitted is scattered. The fraction of the radiation that is not transmitted is described by the terms $(1 - \tau)$ which appear for all four summands. P_{scat} is the scattering phase function, describing the probability of a given scattering angle. ρ_{spec} is the reflectance of the cell surface. ω, τ, and ρ_{spec} are considered to be spectrally weighted averages over the wavelength.

When the drone is flying above the modules, the angle $\theta_{I,I}$ is typically corresponding to backward or sideward scattering while $\theta_{I,II}$ is corresponding to forward scattering. Scattering is strongly direction dependent and after averaging over wavelengths and particle sizes, forward scattering is dominant over other scatter directions. We can ensure that this condition is met by selecting images with a specific geometrical configuration. For this reason, all terms containing $P_{scat}(\theta_{I,I}, \lambda)$ or $P_{scat}(\theta_{II,II}, \lambda)$ are neglected and we consider the equality of $\theta_{I,II}$ and $\theta_{II,I}$ leading to Equation (A13).

$$
\begin{aligned}
L_{\lambda,scat,dir}^{soiled}(\overrightarrow{r_{cam}}, \overrightarrow{r_{sun}}) \\
= L_{\lambda,dir}^{soiled}(\overrightarrow{r_{sun}}) \cdot \omega \cdot \rho_{spec} \cdot P_{scat}(\theta_{I,II}, \lambda) \\
\cdot [(1 - \tau(\alpha_{cam})) \cdot \tau(\alpha_{sun}) + (1 - \tau(\alpha_{sun})) \cdot \tau(\alpha_{cam})]
\end{aligned} \tag{A16}
$$

Equation (A13) is also valid for irradiances instead of radiances when introducing an additional proportionality factor *c*. We obtain Equation (A14).

$$
\begin{aligned}
E_{\lambda,scat,dir}^{soiled}(\overrightarrow{r_{cam}}, \overrightarrow{r_{sun}}) \\
= c \cdot DNI_{\lambda} \cdot \omega \cdot \rho_{spec} \cdot P_{scat}(\theta_{I,II}, \lambda) \\
\cdot [(1 - \tau(\alpha_{cam})) \cdot \tau(\alpha_{sun}) + (1 - \tau(\alpha_{sun})) \cdot \tau(\alpha_{cam})]
\end{aligned} \tag{A17}
$$

The wavelength-dependent irradiance of the scattered direct radiation that hits the pixel sensor is denoted $E_{\lambda,scat,dir}^{soiled}$ and the wavelength-dependent direct normal irradiance that hits the module is denoted DNI_{λ}. Coming back to the calculation of R_{scat}, we can write the following:

$$
\begin{aligned}
R_{scat} &= \int_{\lambda_{min}}^{\lambda_{max}} \varepsilon \cdot E_{\lambda,scat,dir}^{soiled}(\overrightarrow{r_{cam}}, \overrightarrow{r_{sun}})d\lambda \\
&= \int_{\lambda_{min}}^{\lambda_{max}} \varepsilon \cdot c \cdot \omega \cdot \rho_{spec} \cdot DNI_\lambda(\alpha_{sun}) \cdot P_{scat}(\theta_{I,II}, \lambda) \\
&\quad \cdot [(1 - \tau(\alpha_{cam})) \cdot \tau(\alpha_{sun}) + (1 - \tau(\alpha_{sun})) \cdot \tau(\alpha_{cam})]d\lambda
\end{aligned}
\tag{A18}
$$

c, ω, and ρ_{spec} can be combined to a new constant $c\prime$.

$$
\begin{aligned}
R_{scat} &= \\
\int_{\lambda_{min}}^{\lambda_{max}} &c' \cdot \varepsilon \cdot DNI_\lambda(\alpha_{sun}) \cdot P_{scat}(\theta_{I,II}, \lambda) \\
&\cdot [(1 - \tau(\alpha_{cam})) \cdot \tau(\alpha_{sun}) + (1 - \tau(\alpha_{sun})) \cdot \tau(\alpha_{cam})]d\lambda \\
&= c' \cdot [(1 - \tau(\alpha_{cam})) \cdot \tau(\alpha_{sun}) + (1 - \tau(\alpha_{sun})) \cdot \tau(\alpha_{cam})] \\
&\cdot \int_{\lambda_{min}}^{\lambda_{max}} \varepsilon \cdot DNI_\lambda(\alpha_{sun}) \cdot P_{scat}(\theta_{I,II}, \lambda)d\lambda
\end{aligned}
\tag{A19}
$$

In the following step, it is assumed that the remaining integral is proportional to the DNI multiplied by an integral just over ε and P_{scat}. The proportionality factor c' therefore changes to c''.

$$
\begin{aligned}
R_{scat} = c'' \cdot [(1 - \tau(\alpha_{cam})) \cdot \tau(\alpha_{sun}) + (1 - \tau(\alpha_{sun})) \cdot \tau(\alpha_{cam})] \cdot DNI \\
\cdot \int_{\lambda_{min}}^{\lambda_{max}} \varepsilon \cdot P_{scat}(\theta_{I,II}, \lambda)d\lambda
\end{aligned}
\tag{A20}
$$

In a final step, c'' and the integral are combined to define the function $c_{scat}(\overrightarrow{r_{sun}}, \overrightarrow{r_{cam}})$.

$$
\begin{aligned}
R_{scat} = [(1 - \tau(\alpha_{cam})) \cdot \tau(\alpha_{sun}) + (1 - \tau(\alpha_{sun})) \cdot \tau(\alpha_{cam})] \cdot DNI \\
\cdot c_{scat}(\overrightarrow{r_{sun}}, \overrightarrow{r_{cam}})
\end{aligned}
\tag{A21}
$$

The empirical scattering function $c_{scat}(\overrightarrow{r_{sun}}, \overrightarrow{r_{cam}})$ describes the probability of different scattering directions.

Equations (A10) and (A18) can be combined to isolate the empirical scattering function $c_{scat}(\overrightarrow{r_{sun}}, \overrightarrow{r_{cam}})$.

$$
\begin{aligned}
&c_{scat}(\overrightarrow{r_{sun}}, \overrightarrow{r_{cam}}) \\
&= \frac{R_{soiled,GTI,norm} - R_{clean,GTI,norm} \cdot \tau(\alpha_{cam}) \cdot \tau(\alpha_{sun})}{[(1 - \tau(\alpha_{cam})) \cdot \tau(\alpha_{sun}) + (1 - \tau(\alpha_{sun})) \cdot \tau(\alpha_{cam})] \cdot \frac{DNI(t_{soiled})}{GTI(t_{soiled})}}
\end{aligned}
\tag{A22}
$$

Equation (A19) can also be solved for τ_0, the value of the soiling transmission for $\alpha = 0$ when using Equation (A9). All results for the soiling loss later on refer to normal incidence ($\alpha = 0$).

$$
\tau_0 = 1 - \frac{-b + \sqrt{b^2 - 4 \cdot a \cdot d}}{2 \cdot a} \ \ with
$$

$$
a = \frac{R_{clean,GTI,norm} - 2 \cdot c_{scat}(\overrightarrow{r_{sun}}, \overrightarrow{r_{cam}}) \cdot \frac{DNI(t_{soiled})}{GTI(t_{soiled})}}{cos(\alpha_{cam}) \cdot cos(\alpha_{sun})}
\tag{A23}
$$

$$
b = \frac{cos(\alpha_{cam}) + cos(\alpha_{sun})}{cos(\alpha_{cam}) \cdot cos(\alpha_{sun})} \cdot \left(c_{scat}(\overrightarrow{r_{sun}}, \overrightarrow{r_{cam}}) \cdot \frac{DNI(t_{soiled})}{GTI(t_{soiled})} - R_{clean,GTI,norm} \right)
$$

$$
d = R_{clean,GTI,norm} - R_{soiled,GTI,norm}
$$

With this set of equations, it is possible to determine the soiling ratio for a given image as described in the next section. First, images of the clean reference module will be used to calculate the expected background signal corresponding to a clean PV module for any geometry (see Appendix A.2.1). $R_{clean,GTI,norm}$ can then be determined for any camera position. Afterwards, the images of the soiled reference module are analyzed, and using the measured τ_0 for this reference module, c_{scat} can be determined in dependence of the geometry (see Appendix A.2.2). Finally, the soiling loss can be measured for a third module (see Appendix A.2.3).

Appendix A.2. Calibration Measurements for the Determination of the Background Signal and the Conversion of the Brightness Increase to Soiling Losses

Before the method is applied to analyze the soiling losses of a PV module with unknown soiling loss, two calibration measurements are performed with a clean and a soiled module with known soiling loss.

Appendix A.2.1. Determination of Expected Background Signal Corresponding to a Clean PV Module

The goal is to determine the expected background signal corresponding to a clean PV module $R_{clean,GTI,norm}$ in dependence of the geometry defined by $\overrightarrow{r_{cam}}$ and $\overrightarrow{r_{sun}}$. Consequently, before the measurement flight, one module is cleaned. Images of this module are captured from various perspectives, which can be achieved, e.g., using a spiral flight route. Every cell of the clean module is examined individually. For each image and each cell, the geometry and the brightness are determined. $\overrightarrow{r_{cam}}$ and $\overrightarrow{r_{sun}}$ are reduced to the angle between the camera vector and the sun reflex vector $\theta_{cam,sunrefl}$ (the scattering angle) and the angle between the camera vector and the module normal vector $\theta_{cam,panelnorm}$ to describe the geometry. The idea is to model the expected brightness for a clean module as a function of these two angles. Afterwards, the clean brightness can be calculated and subtracted as a background signal for the images of other PV modules that are to be evaluated. The method requires many images from different perspectives. For example, assuming 100 reference images and one clean reference module with 60 cells results in 6000 datapoints consisting of the brightness and the two angles mentioned above.

After filtering the data points as described in the previous section, a polynomial fit of second order is performed to describe $R_{clean,GTI,norm}$ as a function of $\theta_{cam,sunrefl}$ and $\theta_{cam,panelnorm}$. Using this fit, the expected brightness of an imaginary clean module under any geometry can be calculated. The influence of this fit on the calibration is discussed further and visualized in Appendix B.3.1. Note that the same $\theta_{cam,sunrefl}$ can be obtained from various combinations of $\overrightarrow{r_{cam}}$ and $\overrightarrow{r_{sun}}$. This means in particular that even when the sun position has changed over time, we can still compare images of the clean modules with an early timestamp with images of the soiled module with a later timestamp.

Appendix A.2.2. Determination of the Scattering Behavior c_{scat}

The next intermediate goal is to determine c_{scat} in dependence of the geometry defined by $\overrightarrow{r_{cam}}$ and $\overrightarrow{r_{sun}}$. Therefore, the scattering calibration is performed after the clean one. It is required for the evaluation of other modules. One soiled module with known soiling loss is considered. It should be homogeneously soiled, and the soiling losses have to be determined using electrical measurements as described in Section 3.3.2. As in the case of the background signal, many images are captured from various perspectives. In the case that the clean and soiled reference modules are located directly next to each other, one flight is sufficient to perform both calibrations. The geometry is used to determine the clean background signal for each cell and each image. By comparing the actual RGB value of the soiled cells and the clean background values, the brightness increase is determined. Considering the geometry, the electrical soiling loss, the irradiances at the image acquisition times, and the brightness increases enables the calculation of the scattering function c_{scat} according to Equation (A19) from the previous section. First, discrete values are calculated for each cell and image. Afterwards, the scattering function is described in dependence of $\theta_{cam,sunrefl}$ and $\theta_{cam,sun}$, the angle between the camera vector and the sun vector using a polynomial fit of the second order. The influence of this fit on the calibration is discussed further and visualized in Appendix B.3.2.

Appendix A.2.3. Calculation of Soiling Loss

After the calibration $R_{clean,GTI,norm}(\theta_{cam,sunrefl}, \theta_{cam,panelnorm})$ and $c_{scat}(\theta_{cam,sunrefl}, \theta_{cam,sun})$ are known. Now, a flight over the modules for which the soiling loss should be measured can be performed. In case of this study this was a straight-line flight in east-west direction over south-facing modules with 30° tilt, as this is considered practical for measurements of large PV fields. Equation (A20) is then used together with the background signal $R_{clean,GTI,norm}$ and c_{scat} to determine the soiling loss of each cell of the PV modules as seen in each image. One soiling loss value is obtained for every cell and each image. Values for a cell that are deviating by more than two standard deviations from the median for this cell are excluded to reduce the impact of noise and outliers. Afterwards, the arithmetic average is again calculated. Finally, one obtains the soiling loss for each cell as an average of the soiling losses from each image for this cell that remain after the filtering.

Appendix B.

Appendix B.1. Analyses of All Measurements

The analysis of the first flight of the first campaign has been shown in the result section. Here, the other flights of the first campaign and all other campaigns are shown.

Appendix B.1.1. First Campaign Second Flight

Figure A3 summarizes the results of the second flight of the first campaign. The soiling of the first validation module is determined with a deviation of 0.1% absolute. The soiling of the second validation module is determined with a deviation of 1.0% absolute. It should be noted that the second validation module was soiled with a different soiling type than the other modules which explains an increased deviation.
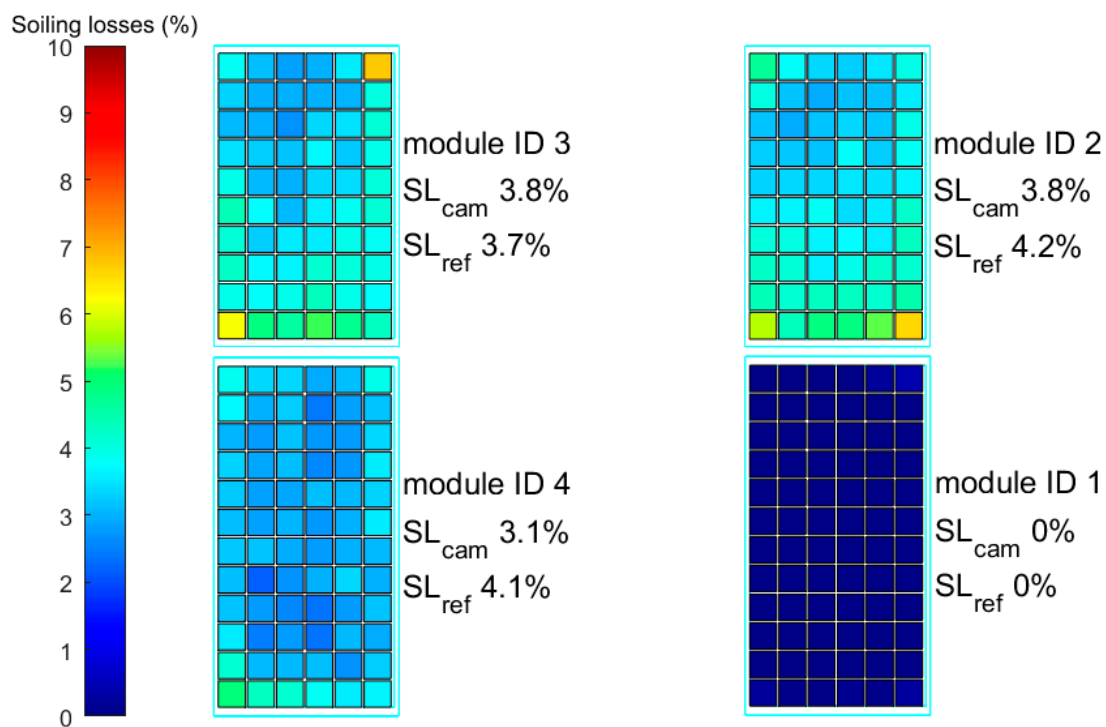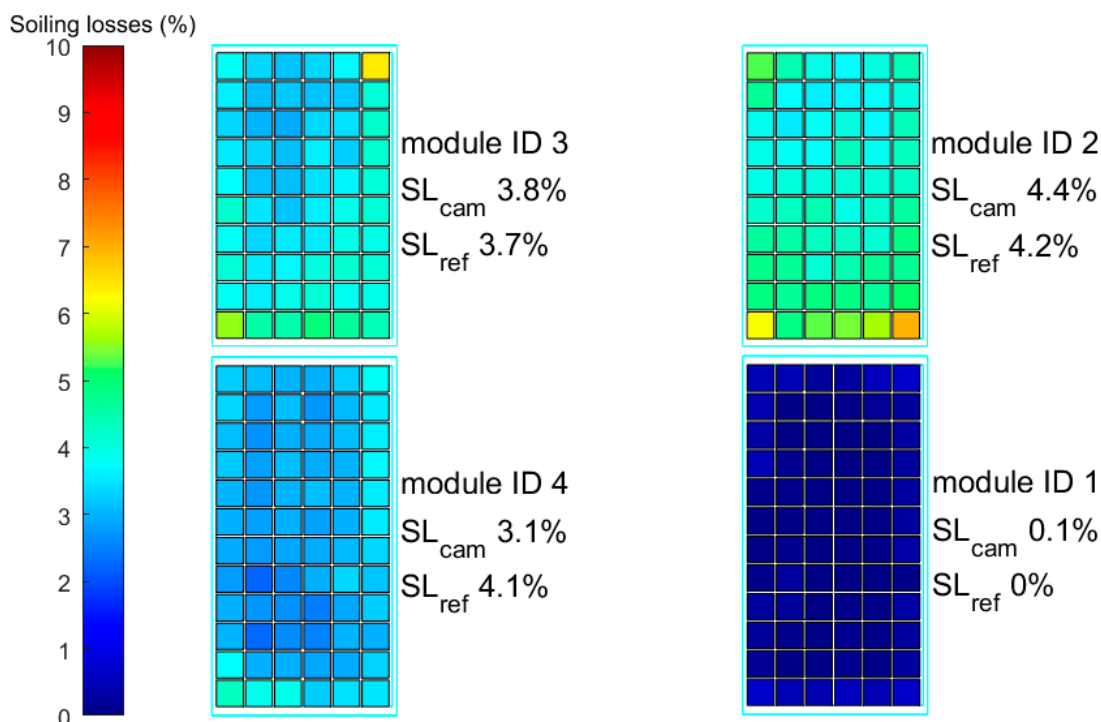

Figure A3. Result plot of the second measurement flight of the first campaign. The lower right module was chosen to be the clean reference module while the upper right module was chosen to be the soiled reference module. The upper numbers label the modules. The number in the middle states the optically measured soiling loss while the lower number is the electrical reference loss.

Appendix B.1.2. First Campaign Third Flight

Figure A4 summarizes the results of the third measurement flight of the first campaign. The soiling of the first validation module is determined with a deviation of 0.1% absolute. The soiling of the second validation module is determined with a deviation of 1.0% absolute. It should be noted that the second validation module was soiled with a different soiling type than the other modules which explains an increased deviation.
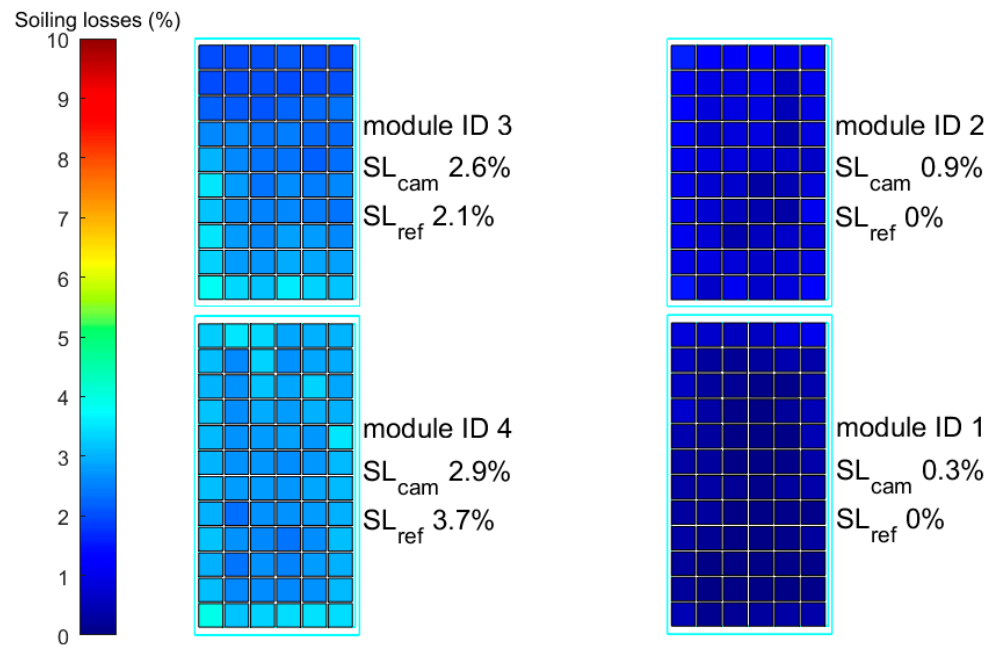

Figure A4. Result plot of the third measurement flight of the first campaign. The lower right module was chosen to be the clean reference module while the upper right module was chosen to be the soiled reference module. The upper numbers label the modules. The number in the middle states the optically measured soiling loss while the lower number is the electrical reference loss.

Appendix B.1.3. First Campaign Fourth Flight

Figure A5 summarizes the results of the fourth measurement flight of the first campaign. The soiling of the first validation module is determined with a deviation of 0.4% absolute. The lower left module was used as second validation module and it was cleaned before the flight. This explains the different soiling loss compared to the other three flights of the same campaign. The soiling of the second validation module is determined with a deviation of 0.3% absolute.

Appendix B.1.4. Second Campaign First Flight

During the second campaign the lower right as well as the upper right module were both clean. Figure A6 shows the setup during the second campaign.

Figure A7 summarizes the results of the first measurement flight of the second campaign. The soiling of the first validation module is determined with a deviation of 0.5% absolute. The soiling of the second validation module is determined with a deviation of 0.9% absolute.
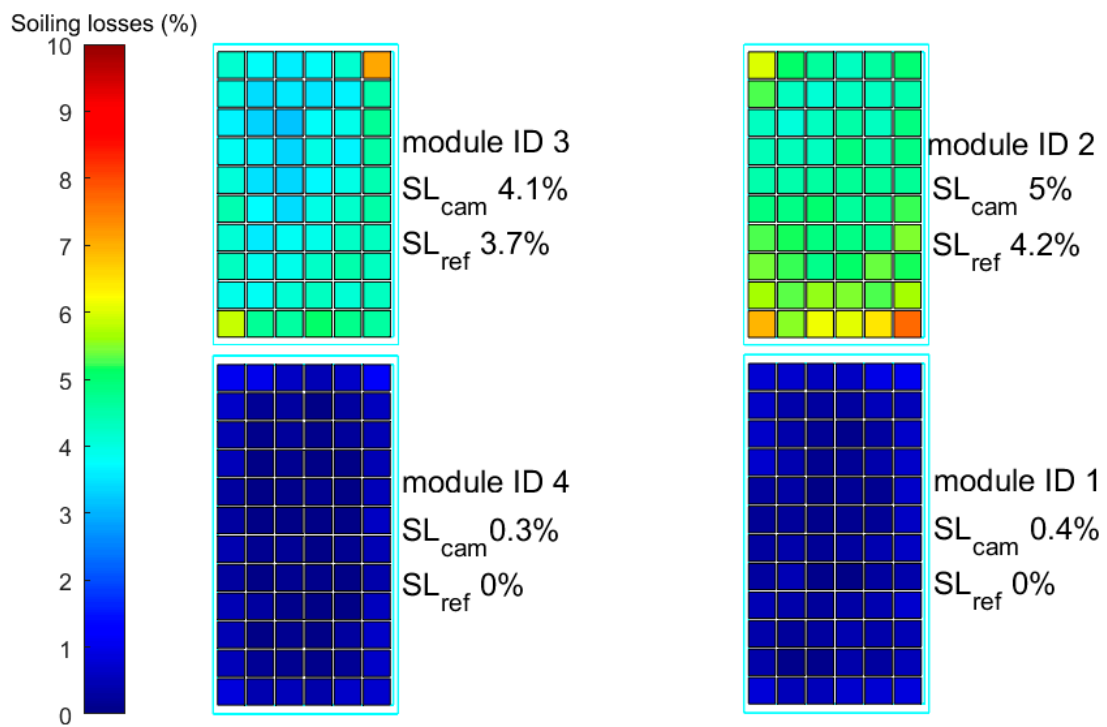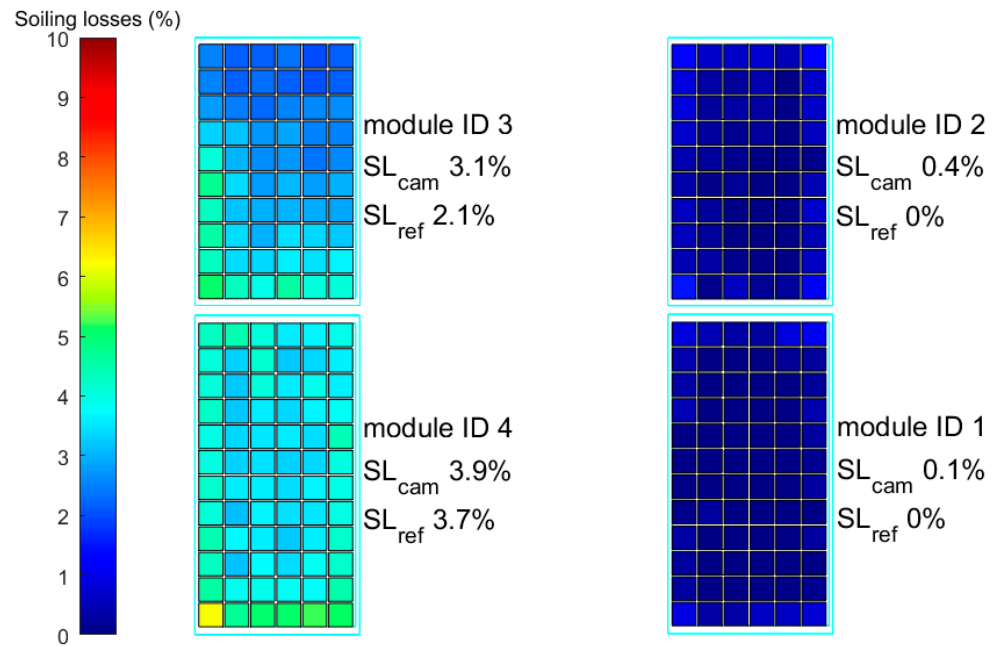
Figure A5. Result plot of the fourth measurement flight of the first campaign. The lower right module was chosen to be the clean reference module while the upper right module was chosen to be the soiled reference module. The lower left module was cleaned before the flight which explains the different soiling loss compared to the other three flights of the same campaign. The upper numbers label the modules. The number in the middle states the optically measured soiling loss while the lower number is the electrical reference loss.

Figure A6. The setup during the second campaign. The modules on the right are both clean. Out of these two, the lower right was used as a clean reference. The lower left module was used as a soiled reference.
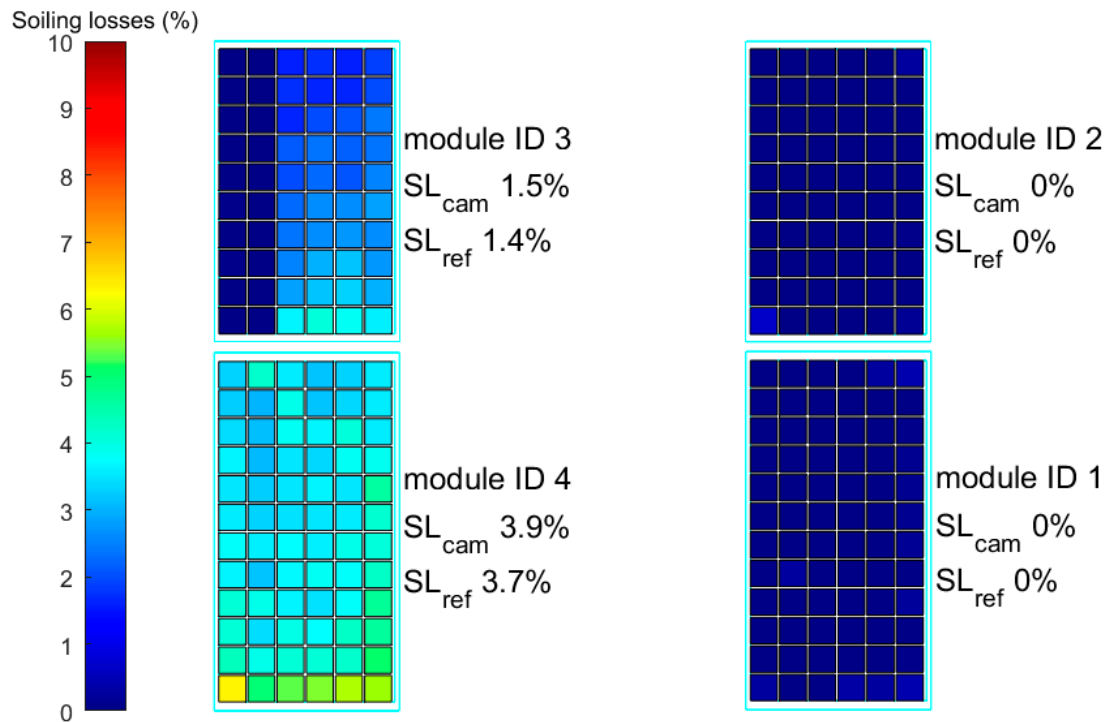
Figure A7. Result plot of the first measurement flight of the second campaign. The lower right module was chosen to be the clean reference module while the lower left module was chosen to be the soiled reference module. The upper numbers label the modules. The number in the middle states the optically measured soiling loss while the lower number is the electrical reference loss.

Appendix B.1.5. Second Campaign Second Flight

Figure A8 summarizes the results of the second measurement flight of the second campaign. The soiling of the first validation module is determined with a deviation of 1.0% absolute. The soiling of the second validation module is determined with a deviation of 0.4% absolute.

Figure A8. Result plot of the second measurement flight of the second campaign. The lower right module was chosen to be the clean reference module while the lower left module was chosen to be the soiled reference module. The upper numbers label the modules. The number in the middle states the optically measured soiling loss while the lower number is the electrical reference loss.

Appendix B.1.6. Second Campaign Third Flight

Figure A9 summarizes the results of the third measurement flight of the second campaign. The left substring of the upper left module was cleaned before the flight (two columns of cells cleaned). The soiling of the first validation module is determined with a deviation of 0.1% absolute. In case of the second validation module, the electrically and optically measured soiling losses are identical.

Figure A9. Result plot of the third measurement flight of the second campaign. The lower right module was chosen to be the clean reference module while the lower left module was chosen to be the soiled reference module. The left substring of the upper left module was cleaned before the flight (two columns of cells cleaned). The upper numbers label the modules. The number in the middle states the optically measured soiling loss while the lower number is the electrical reference loss.

Appendix B.1.7. Third Campaign First Flight

For the third campaign, the modules were artificially soiled with gypsum. The gypsum was mixed with water and the mixture was then deposited on the module with a towel. The operating temperature of the module led to a quick drying of the mixture. The artificial soiling was as homogeneously distributed as possible and was considered to be sufficiently homogeneous by simple visual inspection. After obtaining the results of this measurement, the above-mentioned electrical model confirmed that the soiling was homogeneous enough to neglect additional mismatch losses. Figure A10 shows the artificially soiled setup during the measurement.

Figure A11 summarizes the results of the first measurement flight of the third campaign. The soiling loss of the first validation module is determined with a deviation of 2.3% absolute. The soiling of the second validation module is determined with a deviation of 1.7% absolute.

The larger deviations in this case might be explained by the fact that in this experiment, artificial soiling was used as explained in the discussion of Figure 8.
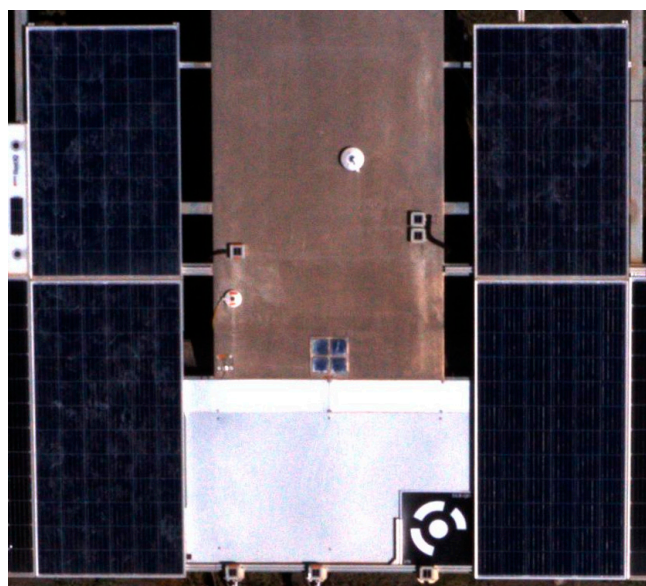
Figure A10. The setup during the third campaign. The modules are artificially soiled. The lower right module was used as a clean reference. The lower left module was used as a soiled reference.
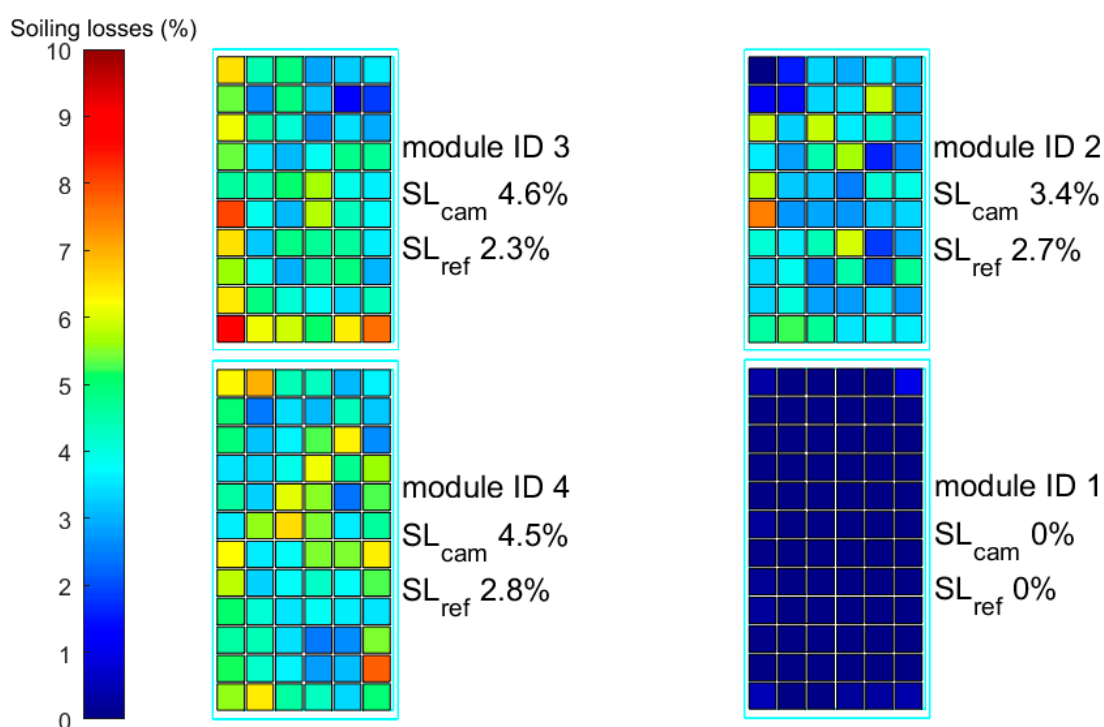

Figure A11. Result plot of the first measurement flight of the third campaign. The lower right module was chosen to be the clean reference module while the upper right module was chosen to be the soiled reference module. In this campaign, the modules were soiled artificially with gypsum. The artificial soiling was not as homogeneously distributed as was the case for the previous campaigns with natural soiling. The upper numbers label the modules. The number in the middle states the optically measured soiling loss while the lower number is the electrical reference loss.

Appendix B.2. Electrical Reference Measurements for All Campaigns

This section summarizes and visualizes the electrical reference measurement of the soiling loss for all three campaigns.

Appendix B.2.1. First Campaign

For the first campaign, the electrical reference of the soiling loss was determined by comparing the modules' power output with the GTI measured by a reference cell. Figure A12 shows the ratio of module power to GTI for a reference day on which both devices were clean. This day is used to calibrate the modules relative to the reference cell. The GTI, the module temperature, and the wind speed at 10 m height are shown in Figure A13 for the reference day and the day of the drone-based soiling measurement. The determined calibration factor is then used to calculate the soiling loss on the measurement day as shown in Figure A14. Module 1 is not shown in either figure because the module was cleaned before the measurement and is therefore defined to have a soiling loss of zero. Note that for the optical calculation of the soiling loss, an angle correction was applied (see Equation (A9)). The same angle correction should be applied for the electrical measurements for the sake of consistency. This was carried out in a test run and it was found that for the electrical measurements, the angle dependence played a neglectable role as the angle of incidence was very close to zero for the time interval of interest. This is due to the modules' inclination of $30°$ and because the electrical measurements took place around solar noon. Furthermore, the experiments took place in April and September, which are months in which the sun reaches around $60°$ elevation at solar noon in Almería. Together with the $30°$ inclination, this leads to nearly perpendicular incidence.

Figure A13 shows in the center the measured module temperature for the measurement day and the reference day. The temperature is measured at module 3 in both cases. It is assumed that the temperature is very similar for all four modules since they are of the same technology, from the same manufacturer, have the same orientation, and experience very similar operating conditions. Especially, it should be noted that the soiling is not significant enough to cause a hotspot. The lower two subfigures of Figure A13 show the wind speed at both days as the wind speed is a key parameter influencing the module temperature.
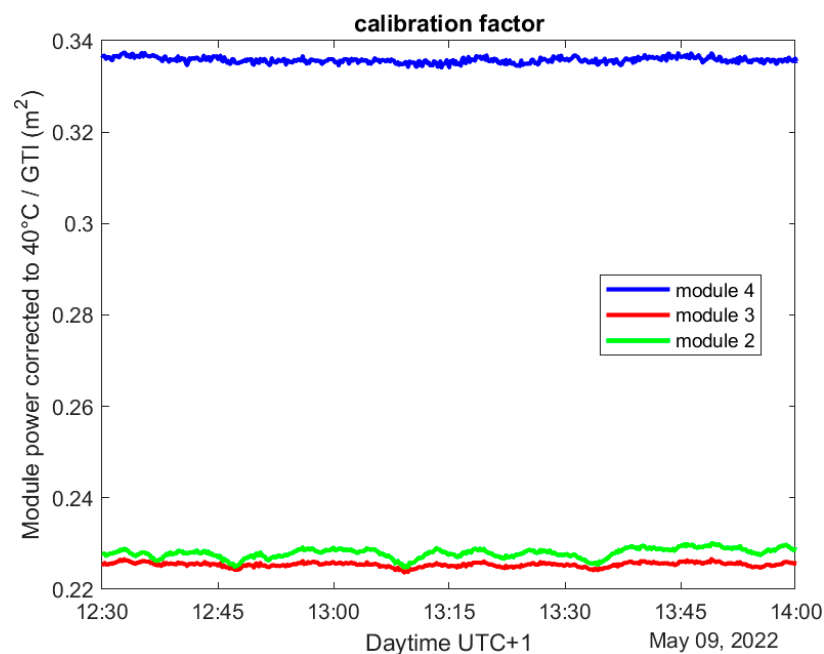

Figure A12. Calibration factor for the electrical calculation of the reference soiling loss for the first campaign measured with clean devices (reference day). The powers of modules 2, 3, and 4 are divided by the GTI measured by a reference cell. The derived calibration factors are 0.228 m^2, 0.2254 m^2, and 0.3248 m^2 for modules 2, 3, and 4, respectively.
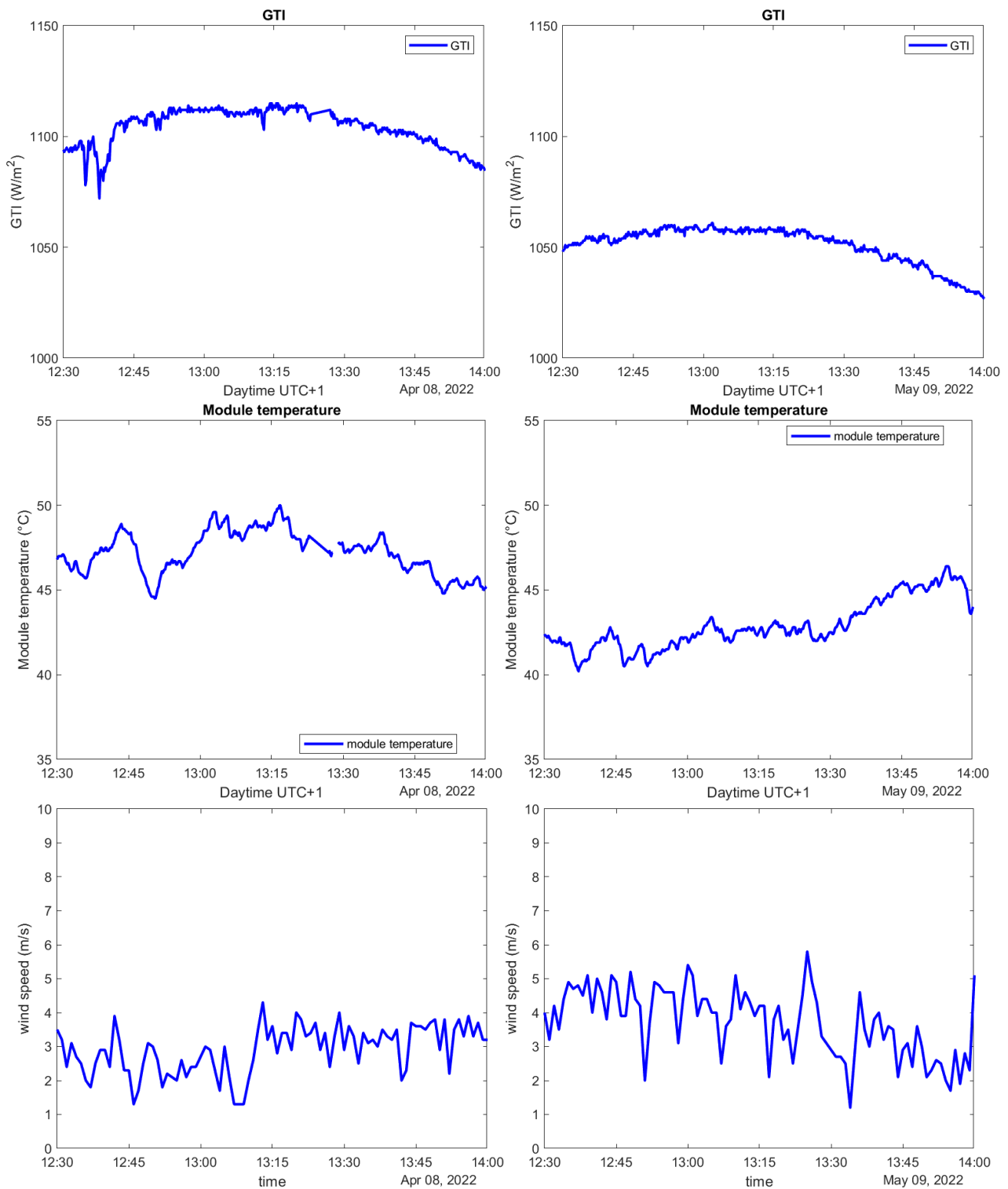
Figure A13. Upper left: GTI at the measurement day, upper right: GTI at the reference day. Center left: Module temperature measured at the measurement day. The average temperature in the chosen time interval is 47.2 °C. Center right: Module temperature at the reference day. The average temperature is 42.9 °C. Lower left: Wind speed at the measurement day. Lower right: Wind speed at the reference day.
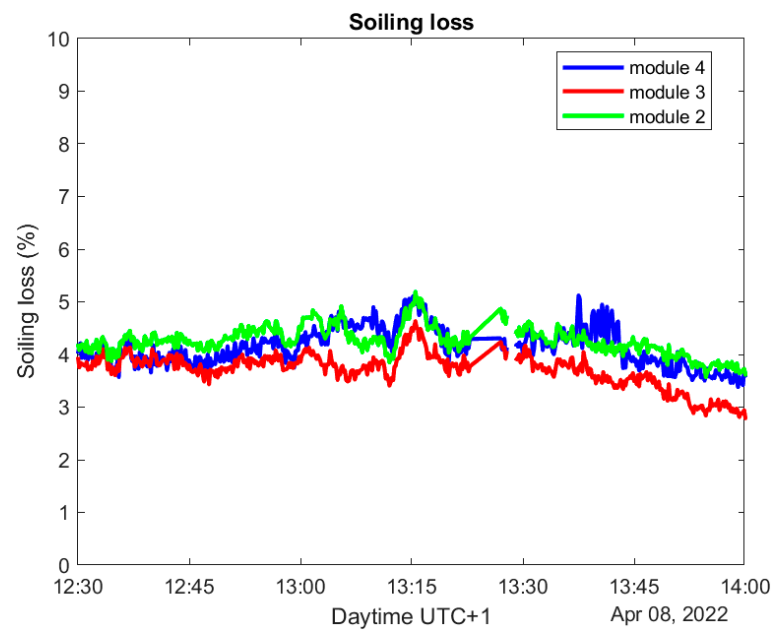
Figure A14. Soiling loss for modules 2, 3, and 4 during the first campaign. The module powers are divided by the GTI and then divided by the previously determined calibration factor. The averaged soiling losses of modules 2, 3, and 4 are 4.2%, 3.7%, and 4.1%, respectively. Data between 13:22 and 13:27 were excluded as the reference cell was shaded by the scientists.

Appendix B.2.2. Second Campaign

For the second campaign, the soiling loss was determined by comparing the powers of the soiled modules with the power of the clean module. Figure A15 shows the ratio of powers for the case in which all modules are clean. The powers of modules 2, 3, and 4 are divided by the power of the clean module 1. Thus, the determined calibration factor is applied to obtain the soiling loss. Figure A16 shows the calculated soiling loss for the measurement day itself.
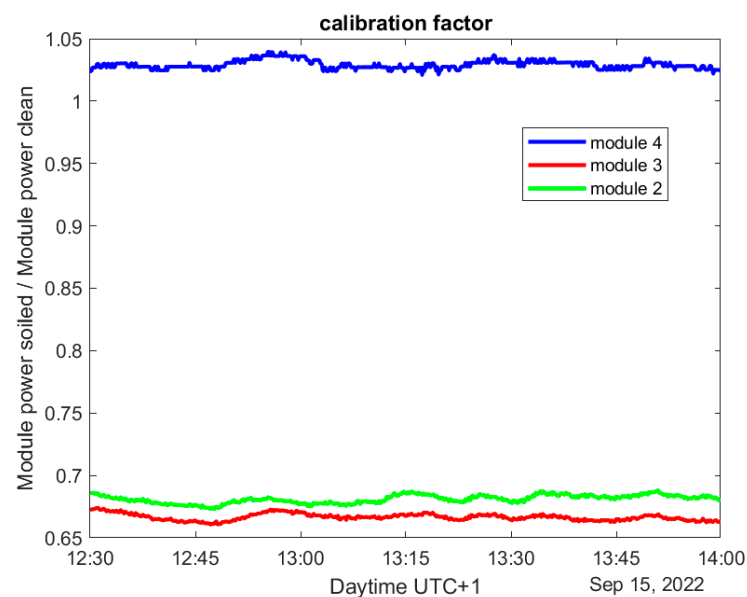
Figure A15. Calibration factors for the electrical calculation of the reference soiling loss for the second campaign. The powers of modules 2, 3, and 4 are divided by the power of module 1 on a day on which all modules are clean. The derived calibration factors are 0.681, 0.6666, and 1.0291 for modules 2, 3, and 4, respectively.
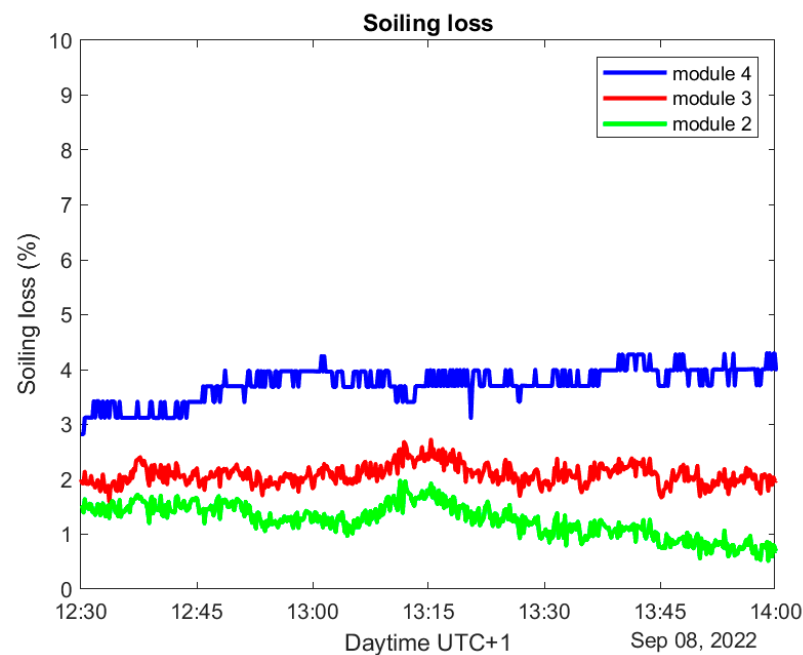
Figure A16. Calculation of the soiling loss for modules 2, 3, and 4 during the second campaign. The module powers are divided by the power of module 1 and then divided by the previously determined calibration factor. The calculated soiling losses are 1.25%, 2.09%, and 3.75% for modules 2, 3, and 4, respectively.

Appendix B.2.3. Third Campaign

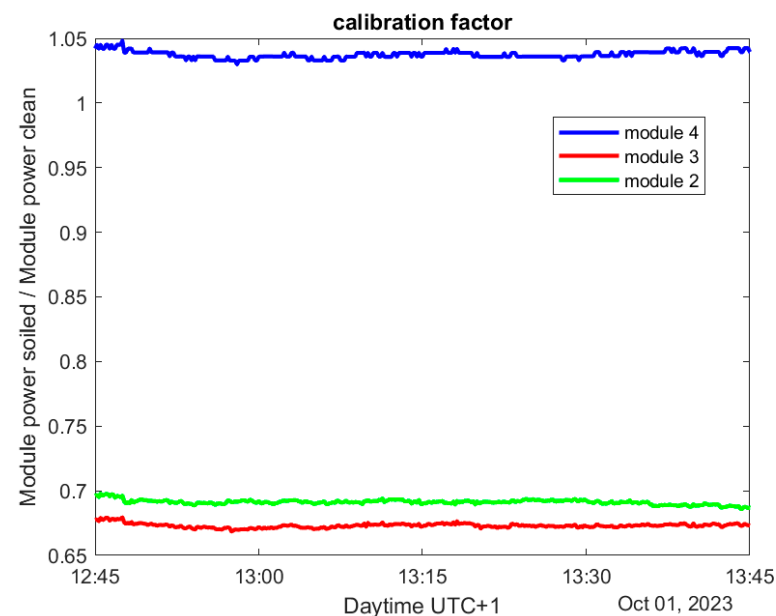The soiling loss is determined analogous to the second campaign (see Appendix A.2.2).

Figure A17. Calibration factors for the electrical calculation of the reference soiling loss for the third campaign. The powers of modules 2, 3, and 4 are divided by the power of module 1 on a day on which all modules are clean. The derived calibration factors are 0.6911, 0.6729, and 1.0373 for modules 2, 3, and 4, respectively.
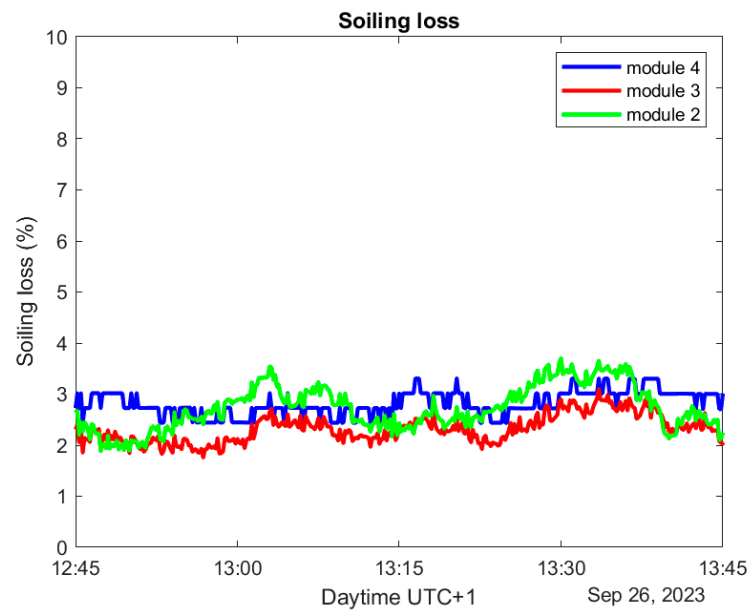
Figure A18. Calculation of the soiling loss for modules 2, 3, and 4 during the third campaign. The module powers are divided by the power of module 1 and then divided by the previously determined calibration factor. The calculated soiling losses are 2.72%, 2.32%, and 2.82% for modules 2, 3, and 4, respectively.

Appendix B.3. Visualization of the Calibration Functions

In this section, the calibration of the clean background signal and the calibration of the scattering signal are described. As an example, we choose to show the calibrations of the first flight of the first campaign which correspond to the results shown in Section 4 in the main part.

Appendix B.3.1. Clean Background Calibration

After performing the calibration flight, one obtains the brightnesses of the cells of the clean module. The brightnesses are averaged over the cells' areas and are then normalized to the exposure time and to the GTI present at the time of capturing the image. These normalized brightnesses are then available for different cells, camera positions, and different sun positions. Figure A19 visualizes the second-order polynomial fit that is performed to describe the normalized brightness in terms of $\theta_{cam,sunrefl}$ and $\theta_{cam,panelnorm}$.

Figure A20 shows the relative deviations between the normalized brightnesses that are used to create the clean background calibration and the brightnesses that would be expected according to the polynomial function (the fit values are subtracted from the measured values and divided by the fit values). For every image, we obtain 72 data points since the clean module has 72 cells. These 72 cells have very similar angles as they are spatially very close to each other. The deviations between different cells from the same image are roughly on the same level as deviations for the same cell but from the next image. The fact that some cells within a given image show different brightnesses than others can be attributed to the fact that some cells are slightly brighter or darker than others in reality. Also, the masking of cell in-between spaces cannot be performed perfectly so that this space might influence some cells more than others. There is no sharp edge between the cell and the in-between space in the images. Rather, there is a continuous drop in brightness when one moves from the in-between space towards the cell.

The relative deviation of 30% observed for some points in Figure A20 might seem alarming at first. By analyzing Equation (A20), one can see that it is less dramatic than it seems at first glance. The coefficient d depends on the clean calibration value $R_{clean,GTI,norm}$ and on $R_{soiled,GTI,norm}$. However, as an example for a soiling loss of 5%, $R_{soiled,GTI,norm}$ is

typically three times bigger than $R_{clean,GTI,norm}$ so that the relative deviation for d will be less than 30%. In the equations for a and b, the factor $\frac{DNI(t_{soiled})}{GTI(t_{soiled})}$ is relatively close to 1. Both equations are dominated by c_{scat} which is typically 10 times bigger than $R_{clean,GTI,norm}$ as one can extract from Figures A19 and A21, so that the relative deviation for a and b will be significantly below 30%. Finally, one obtains also that the deviation for τ_0 will be less than 30%.
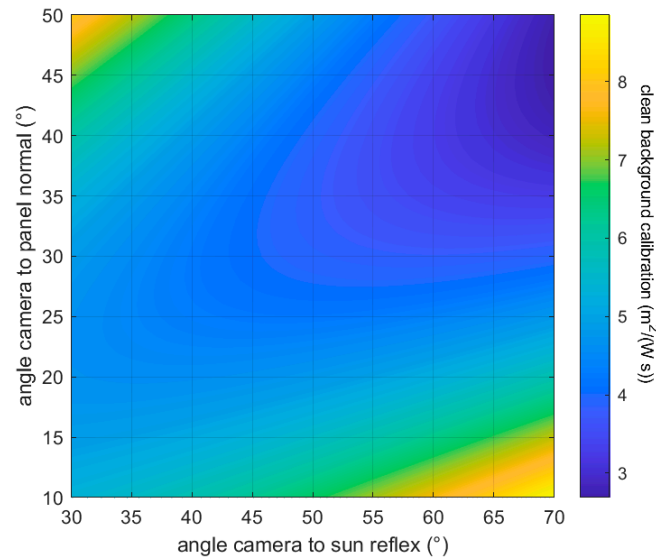

Figure A19. Clean background calibration for the first measurement flight of the first campaign. The x-axis shows the angle between camera and sun reflex vector $\theta_{cam,sunrefl}$ while the y-axis shows the angle between camera vector and panel normal vector $\theta_{cam,panelnorm}$. The calibration function is a polynomial of second order of the above-mentioned angles. The calibration function gives basically the expected brightness normalized to GTI and exposure time, which explains the unit.
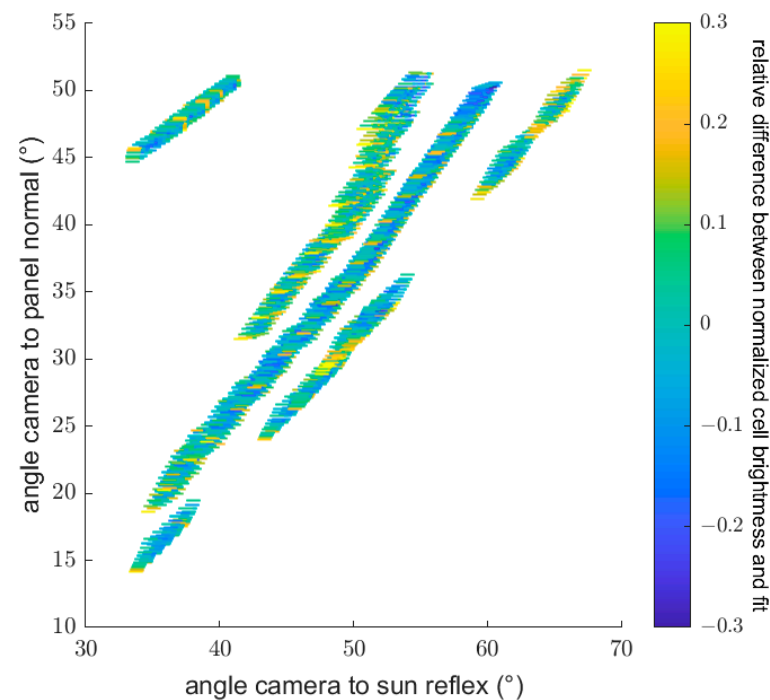

Figure A20. Relative difference between the normalized brightnesses that are used to create the clean background calibration and the expected values according to the fit.
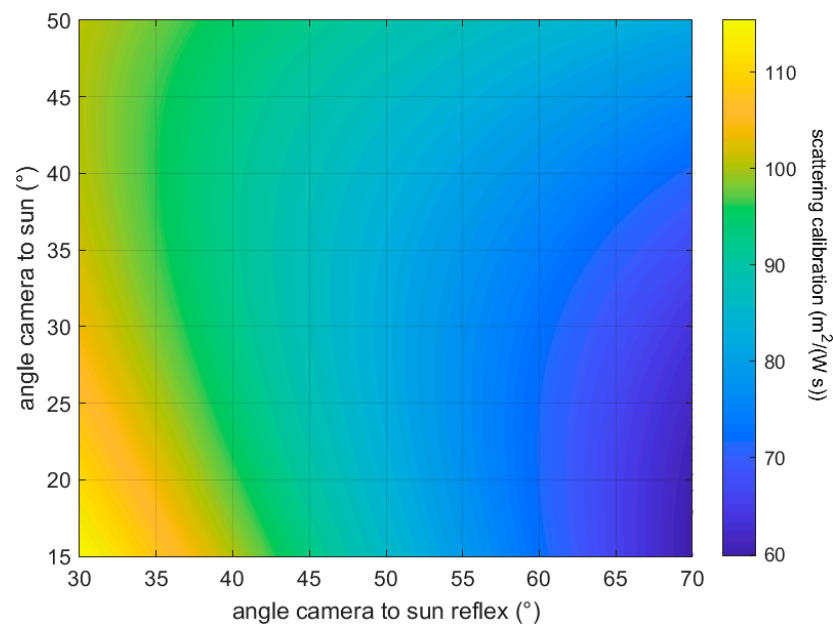
Figure A21. Scattering calibration of the first flight of the first campaign. The x-axis shows the angle between camera vector and sun reflex vector $\theta_{cam,sunrefl}$ while the y-axis shows the angle between camera vector and sun vector $\theta_{cam,sun}$. The color bar shows the scattering calibration parameter c_{scat}.

Appendix B.3.2. Scattering Calibration

After performing the calibration flight, one obtains images of the cells of the soiled reference module from various perspectives. As these perspectives, the soiling loss of this module, and the clean background calibration are already known, one can use Equation (A19) from Appendix A.1.4 to calculate the discrete values of the scattering calibration function c_{scat} for each cell and image. It is assumed as an approximation that the module is homogeneously soiled and that the reference soiling loss on the module level can be used for every cell. Hence, we obtain a data point for each cell and image. Then, a polynomial fit of the second order is created to describe the scattering behavior as a function of $\theta_{cam,sunrefl}$ and $\theta_{cam,sun}$. Figure A21 visualizes this polynomial.

Figure A22 shows the relative differences between the discrete scattering values that were used to create the fit and the values that would be expected according to the fit itself. One can see that the fit in general describes the data quite well. On the other hand, it is observed that on the edge of each of the line shapes' point groups in the figure, there are some points with a higher positive deviation. This indicates that for some of the outer cells in the module, the deviations are higher than for the others. This is explasssined by the module not being exactly homogeneously soiled as assumed when using the same τ_0 for all cells for the calculation of c_{scat}. Figures 5 and 7 confirm that the lower row of cells in module 2 is slightly more soiled than the other cells in the module. We must be aware of this limitation of the method which helps us to understand the found deviations. However, the relatively low deviations shown in Figure 8 indicate that the homogeneity of the soiling of the soiled reference modules was low enough for the reported measurement campaigns to obtain useful results. Also, the electrical data are only available on the module level and using this soiling loss for each cell is only an estimate of the reference soiling loss on the cell level. In case the soiling of the soiled reference module is too inhomogeneous, an iterative determination of c_{scat} could be used.
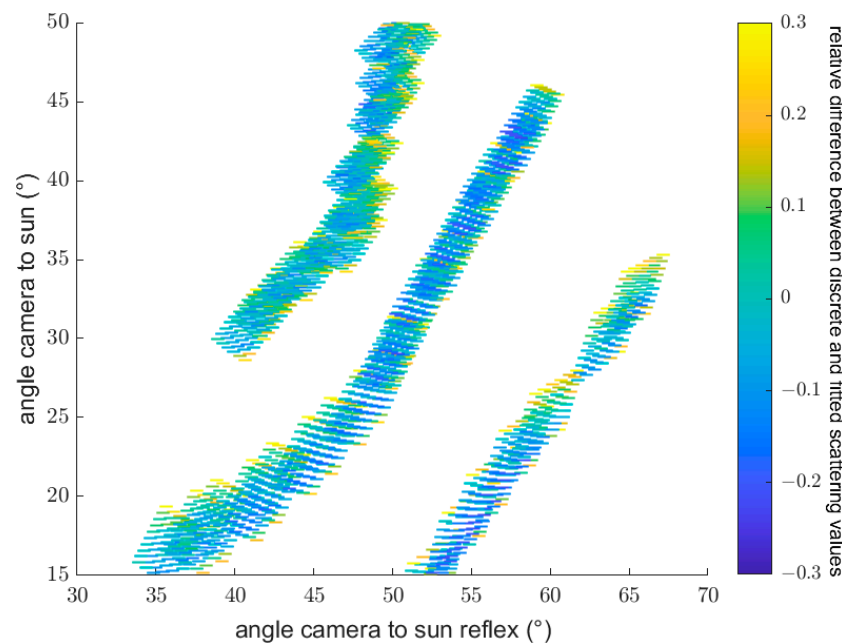
Figure A22. Relative difference between the discrete scattering values and the scattering values expected according to the scattering calibration function.

References

1. Bouckaert, S.; Pales, A.F.; McGlade, C.; Remme, U.; Wanner, B.; Varro, L.; D'Ambrosio, D.; Spencer, T. *Net Zero by 2050: A Roadmap for the Global Energy Sector*; International Energy Agency (IEA): Paris, France, 2021; p. 224.
2. Gielen, D.; Gorini, R.; Wagner, N.; Leme, R.; Gutierrez, L.; Prakash, G.; Asmelash, E.; Janeiro, L.; Gallina, G.; Vale, G.; et al. *Global Energy Transformation: A Roadmap to 2050*; IRENA, International Energy Agency: Masdar City, Abu Dhabi, 2019; p. 52.
3. Ilse, K.; Micheli, L.; Figgis, B.W.; Lange, K.; Daßler, D.; Hanifi, H.; Wolfertstetter, F.; Naumann, V.; Hagendorf, C.; Gottschalg, R.; et al. Techno-economic assessment of soiling losses and mitigation strategies for solar power generation. *Joule* **2019**, *3*, 2303–2321. [CrossRef]
4. Darwish, Z.A.; Kazem, H.A.; Sopian, K.; Alghoul, M.A.; Chaichan, M.T. Impact of some environmental variables with dust on solar photovoltaic (PV) performance: Review and research status. *Int. J. Energy Environ.* **2013**, *7*, 152–159.
5. Vumbugwa, M.; McCleland, J.C.; Van Dyk, E.; Vorster, F.; Serameng, T. Effects of current mismatch due to uneven soiling on the performance of multi-crystalline silicon module strings. *J. Energy S. Afr.* **2020**, *31*, 62–72. [CrossRef]
6. Ma, M.; Liu, H.; Zhang, Z.; Yun, P.; Liu, F. Rapid diagnosis of hot spot failure of crystalline silicon PV module based on IV curve. *Microelectron. Reliab.* **2019**, *100*, 113402. [CrossRef]
7. Schill, C.; Brachmann, S.; Koehl, M. Impact of soiling on IV-curves and efficiency of PV-modules. *Sol. Energy* **2015**, *112*, 259–262. [CrossRef]
8. Chen, D.; Contreras, M.V.; Ciesla, A.; Hamer, P.; Hallam, B.; Abbott, M.; Chan, C. Progress in the understanding of light-and elevated temperature-induced degradation in silicon solar cells: A review. *Prog. Photovolt. Res. Appl.* **2021**, *29*, 1180–1201. [CrossRef]
9. de Oliveira, M.C.; Cardoso, A.S.; Viana, M.M.; Lins, V.D. The causes and effects of degradation of encapsulant ethylene vinyl acetate copolymer (EVA) in crystalline silicon photovoltaic modules: A review. *Renew. Sustain. Energy Rev.* **2018**, *81*, 2299–2317. [CrossRef]
10. García, M.C.A.; Herrmann, W.; Böhmer, W.; Proisy, B. Thermal and electrical effects caused by outdoor hot-spot testing in associations of photovoltaic cells. *Prog. Photovolt. Res. Appl.* **2003**, *11*, 293–307. [CrossRef]
11. Wendlandt, S.; Drobisch, A.; Buseth, T.; Krauter, S.; Grunow, P. Hot spot risk analysis on silicon cell modules. In Proceedings of the 25th European Photovoltaic Solar Energy Conference and Exhibition, Valencia, Spain, 6–10 September 2010.
12. Yang, H.; Xu, W.; Wang, H.; Narayanan, M. Investigation of reverse current for crystalline silicon solar cells—New concept for a test standard about the reverse current. In Proceedings of the 2010 35th IEEE Photovoltaic Specialists Conference, Honolulu, HI, USA, 20–25 June 2010.
13. Dhoke, A.; Sharma, R.; Saha, T.K. Condition monitoring of a large-scale PV power plant in Australia. In Proceedings of the 2016 IEEE Power and Energy Society General Meeting (PESGM), Boston, MA, USA, 17–21 July 2016.
14. Firth, S.; Lomas, K.; Rees, S. A simple model of PV system performance and its use in fault detection. *Sol. Energy* **2010**, *84*, 624–6355. [CrossRef]

15. Micheli, L.; Fernández, E.F.; Fernández-Solas, Á.; Bessa, J.G.; Almonacid, F. Analysis and mitigation of nonuniform soiling distribution on utility-scale photovoltaic systems. *Prog. Photovolt. Res. Appl.* **2022**, *30*, 211–228. [CrossRef]
16. Gostein, M.; Littmann, B.; Caron, J.R.; Dunn, L. Comparing PV power plant soiling measurements extracted from PV module irradiance and power measurements. In Proceedings of the 2013 IEEE 39th Photovoltaic Specialists Conference (PVSC), Tampa, FL, USA, 16–21 June 2013.
17. Gostein, M.; Caron, J.R.; Littmann, B. Measuring soiling losses at utility-scale PV power plants. In Proceedings of the 2014 IEEE 40th Photovoltaic Specialist Conference (PVSC), Denver, CO, USA, 8–13 June 2014.
18. Gostein, M.; Duster, T.; Thuman, C. Accurately measuring PV soiling losses with soiling station employing module power measurements. In Proceedings of the 2015 IEEE 42nd Photovoltaic Specialist Conference (PVSC), New Orleans, LA, USA, 14–19 June 2015.
19. Figgis, B.; Ennaoui, A.; Ahzi, S.; Rémond, Y. Review of PV soiling measurement methods. In Proceedings of the 2016 International Renewable and Sustainable Energy Conference (IRSEC), Marrakech, Morocco, 14–17 November 2016.
20. Wolfertstetter, F.; Esquelli, A.; Wilbert, S.; Hanrieder, N.; Blum, N.; Korevaar, M.; Bergmans, T.; Zarzalejo, L.; Polo, J.; Alami-Merrouni, A.; et al. Incidence angle and diffuse radiation adaptation of soiling ratio measurements of indirect optical soiling sensors. *J. Renew. Sustain. Energy* **2021**, *13*, 033703. [CrossRef]
21. Micheli, L.; Muller, M. An investigation of the key parameters for predicting PV soiling losses. *Prog. Photovolt. Res. Appl.* **2017**, *25*, 291–307. [CrossRef]
22. Alsafasfeh, M.; Abdel-Qader, I.; Bazuin, B.; Alsafasfeh, Q.; Su, W. Unsupervised fault detection and analysis for large photovoltaic systems using drones and machine vision. *Energies* **2018**, *11*, 2252. [CrossRef]
23. Niazi, K.; Akhtar, W.; Khan, H.A.; Sohaib, S.; Nasir, A.K. Binary classification of defective solar PV modules using thermography. In Proceedings of the 2018 IEEE 7th World Conference on Photovoltaic Energy Conversion (WCPEC) (A Joint Conference of 45th IEEE PVSC, 28th PVSEC & 34th EU PVSEC), Waikoloa, HI, USA, 10–15 June 2018.
24. Wu, J.; Chan, E.; Yadav, R.; Gopalakrishna, H.; TamizhMani, G. Durability evaluation of PV modules using image processing tools. In Proceedings of the New Concepts in Solar and Thermal Radiation Conversion and Reliability, San Diego, CA, USA, 19–21 August 2018.
25. Buerhop, C.; Schlegel, D.; Niess, M.; Vodermayer, C.; Weißmann, R.; Brabec, C. Reliability of IR-imaging of PV-plants under operating conditions. *Sol. Energy Mater. Sol. Cells* **2012**, *107*, 154–164. [CrossRef]
26. Qasem, H.; Mnatsakanyan, A.; Banda, P. Assessing dust on PV modules using image processing techniques. In Proceedings of the 2016 IEEE 43rd Photovoltaic Specialists Conference (PVSC), Portland, OR, USA, 5–10 June 2016.
27. Akram, M.W.; Li, G.; Jin, Y.; Chen, X.; Zhu, C.; Zhao, X.; Khaliq, A.; Faheem, M.; Ahmad, A. CNN based automatic detection of photovoltaic cell defects in electroluminescence images. *Energy* **2019**, *189*, 116319. [CrossRef]
28. Yap, W.K.; Galet, R.; Yeo, K.C. Quantitative analysis of dust and soiling on solar pv panels in the tropics utilizing image-processing methods. In Proceedings of the Asia-Pacific Solar Research Conference, Sydney, Australia, 3–5 December 2015.
29. Yfantis, E.; Fayed, A. A camera system for detecting dust and other deposits on solar panels. *Adv. Image Video Process.* **2014**, *2*, 1–10. [CrossRef]
30. Li, X.; Yang, Q.; Chen, Z.; Luo, X.; Yan, W. Visible defects detection based on UAV-based inspection in large-scale photovoltaic systems. *IET Renew. Power Gener.* **2017**, *11*, 1234–1244. [CrossRef]
31. Hwang, P.C.; Ku, C.C.-Y.; Chan, J.C.-C. Soiling detection for photovoltaic modules based on an intelligent method with image processing. In Proceedings of the 2020 IEEE International Conference on Consumer Electronics-Taiwan (ICCE-Taiwan), Taoyuan, Taiwan, 28–30 September 2020.
32. Cavieres, R.; Barraza, R.; Estay, D.; Bilbao, J.; Valdivia-Lefort, P. Automatic soiling and partial shading assessment on PV modules through RGB images analysis. *Appl. Energy* **2022**, *306*, 117964. [CrossRef]
33. Mehta, S.; Azad, A.P.; Chemmengath, S.A.; Raykar, V.; Kalyanaraman, S. Deepsolareye: Power loss prediction and weakly supervised soiling localization via fully convolutional networks for solar panels. In Proceedings of the 2018 IEEE Winter Conference on Applications of Computer Vision (WACV), Lake Tahoe, NV, USA, 12–15 March 2018.
34. Yang, M.; Javed, W.; Guo, B.; Ji, J. Estimating PV Soiling Loss Using Panel Images and a Feature-Based Regression Model. *IEEE J. Photovolt.* **2024**, *14*, 661–668. [CrossRef]
35. Gostein, M.; Stueve, B.; Brophy, B.; Jung, K.; Martinez-Morales, A.; Zhang, S.; Jin, Y.; Xu, J. Soiling measurement station to evaluate anti-soiling properties of PV module coatings. In Proceedings of the 2016 IEEE 43rd Photovoltaic Specialists Conference (PVSC), Portland, OR, USA, 5–10 June 2016.
36. Holmgren, W.F.; Andrews, R.W.; Lorenzo, A.T.; Stein, J.S. PVLIB python 2015. In Proceedings of the 2015 IEEE 42nd Photovoltaic Specialist Conference (PVSC), New Orleans, LA, USA, 14–19 June 2015.
37. Holmgren, W.F.; Hansen, C.W.; Mikofski, M.A. pvlib python: A python package for modeling solar energy systems. *J. Open Source Softw.* **2018**, *3*, 884. [CrossRef]
38. Prahl, C. Photogrammetric Measurement of the Optical Performance of Parabolic Trough Solar Fields. Ph.D. Thesis, RWTH Aachen, Aachen, Germany, 2019.
39. Dunn, L.; Littmann, B.; Caron, J.R.; Gostein, M. PV module soiling measurement uncertainty analysis. In Proceedings of the 2013 IEEE 39th Photovoltaic Specialists Conference (PVSC), Tampa, FL, USA, 16–21 June 2013.

40.   Peterson, J.; Chard, J.; Robinson, J. Extraction of Prevailing Soiling Rates from Soiling Measurement Data. In Proceedings of the 2022 IEEE 49th Photovoltaics Specialists Conference (PVSC), Philadelphia, PA, USA, 5–10 June 2022.
41.   Kuhn, P.; Wilbert, S.; Prahl, C.; Schüler, D.; Haase, T.; Hirsch, T.; Wittmann, M.; Ramirez, L.; Zarzalejo, L.; Meyer, A.; et al. Shadow camera system for the generation of solar irradiance maps. *Sol. Energy* **2017**, *157*, 157–170. [CrossRef]
42.   Wilbert, S. Weiterentwicklung Eines Optischen Messsystems zur Bestimmung der Formabweichungen von Konzentratoren Solarthermischer Kraftwerke unter Dynamischem Windeinfluss. Ph.D. Thesis, DLR/Universität, Bonn, Germany, 2009.
43.   Heimsath, A.; Nitz, P. The effect of soiling on the reflectance of solar reflector materials-Model for prediction of incidence angle dependent reflectance and attenuation due to dust deposition. *Sol. Energy Mater. Sol. Cells* **2019**, *195*, 258–268. [CrossRef]